Energy Conversion and Management 294 (2023) 117564

Contents lists available at ScienceDirect

Energy Conversion and Management

journal homepage: www.elsevier.com/locate/enconman

An analytical approach to converting vibration signal to combustion characteristics of homogeneous charge compression ignition engines

Jacek Hunicz [a,*], Michał S. Gęca [a], Elżbieta Ratajczyk [b], Amin Mahmoudzadeh Andwari [c], Liping Yang [d], Maciej Mikulski [e]

[a] Lublin University of Technology, Faculty of Mechanical Engineering, Nadbystrzycka 36, 20-618 Lublin, Poland
[b] Lublin University of Technology, Faculty of Electrical Engineering and Computer Science, Nadbystrzycka 38A, 20-618 Lublin, Poland
[c] University of Oulu, Machine and Vehicle Design (MVD), Materials and Mechanical Engineering, FI-90014 Oulu, Finland
[d] Harbin Engineering University, College of Power and Energy Engineering, No.145 Nantong Street, Nangang District, Harbin, China
[e] University of Vaasa, School of Technology and Innovation, Wolffintie 34, FI-65200 Vaasa, Finland

ARTICLE INFO

Keywords:
Combustion engine
Vibration
Low-temperature combustion
Combustion analysis

ABSTRACT

Homogeneous charge compression ignition (HCCI) is a promising low-temperature combustion technique for low-emission internal combustion engines. Unlike conventional engines, HCCI lacks a direct ignition control mechanism, necessitating closed-loop combustion control. This study proposes a phenomenological-based, cost-effective, and non-intrusive approach using vibration data analysis to determine essential combustion parameters. Experiments were conducted on a single-cylinder research engine with an accelerometer attached to the engine head. The engine operation envelope covered the whole engine's operating area in naturally aspirated HCCI mode. Wavelet analysis revealed that combustion-related frequencies centered around 500 Hz, independent of operating conditions. The correlation-seeking analysis included peak acceleration amplitude and its crank angle with peak heat release rate (HRR) data. The peak HRR location was accurately identified within one degree when vibration amplitude exceeded the 100 m/s2 threshold. This encompassed 98.5% of the analyzed combustion cycles. The peak HRR prediction accuracy had a maximum error below 21% and was suitable to monitor reaction rates, especially in incomplete combustion and high ringing cycles.

1. Introduction

Despite increasing adoption of new-energy powertrains, internal combustion engines remain ubiquitous in long-haul and marine transport sectors, for heavy-duty working machines and distributed energy generation [1]. Most prospective, next-generation engine concepts are based on the low-temperature combustion (LTC) principle. LTC is achieved by volumetric combustion of a highly-diluted, nearly-homogeneous air–fuel mixture, initiated by compression ignition. The nature of this phenomenon results in a rapid heat release rate (HRR) that is close to an ideal Otto cycle, moving thermodynamic efficiency close to its theoretical boundaries. Furthermore, LTĆs ultra-low emissions, together with its inherited fuel flexibility, are enablers for combustion engine sustainability [2]. Fuel flexibility opens new perspectives for wide applications of alternative fuels. The fuel aspect will not be discussed in detail in the paper. It is sufficient to mention that to date, LTC research has encompassed an abundant range of engine fuels and their various mixtures [3,4].

Homogeneous charge compression ignition (HCCI) combustion is phenomenologically most coherent with the assumptions of LTC and, as such, has been extensively investigated [5]. Unlike conventional compression ignition (CI) combustion, HCCI lacks a direct ignition control mechanism. Achieving a uniform charge requires preparing the air–fuel mixture in the intake runner or cylinder via early injection, which separates injection and auto-ignition. Thus, combustion starts spontaneously, determined by in-cylinder temperature and fuel reactivity [6]. Key challenges in HCCI development are control complexity and high pressure rise rates (PRR) due to volumetric combustion, especially at high engine loads. Development of robust combustion control is, therefore, the endeavour of contemporary HCCI research [7] with special focus on engine operation in transient conditions [8].

HCCI control strategies include thermal conditioning of intake air, variable compression ratio as well as external and internal exhaust gas recirculation (EGR). The latter can be achieved by sophisticated valve

* Corresponding author.
E-mail address: j.hunicz@pollub.pl (J. Hunicz).

https://doi.org/10.1016/j.enconman.2023.117564
Received 14 June 2023; Received in revised form 8 August 2023; Accepted 18 August 2023
Available online 23 August 2023

timing strategies, resulting in exhaust gas rebreathing or exhaust gas trapping and recompression by means of so-called negative valve overlap (NVO) [9]. Furthermore, thermal and compositional stratification of the in-cylinder charge can be controlled effectively by direct fuel injection. Other measures include direct water injection to control in-cylinder temperature and its distribution [10].

On the fuel reactivity side, LTC control approaches include mixing two fuels with different octane numbers or enabling reactivity stratification in the cylinder by taking advantage of two separate fuel injection systems. The second approach, termed reactivity-controlled compression ignition (RCCI) [11], can employ various fuels, also mixed with water to extend the reactivity span [12].

Finally, external and internal fuel reforming should be mentioned as techniques to vary fuel reactivity. External reforming usally takes place in special reactors built into EGR loops, where reactions of hydrocarbon fuel and exhaust produce syngas, a mixture of hydrogen and carbon monoxide [13]. Aside from modifying the mixture reactivity, this method also utilises exhaust gas thermal energy to increase the mixturés heating value, thus improving engine thermal efficiency. Internal (in-cylinder) reforming, involves direct fuel injection into hot residual gasses recompressed during the NVO period. Depending on the valve timing and the start of injection, the fuel cracking produces different active species which improves mixture reactivity. This technique has substantial thermal effects which influence the main event combustion to a large extent [14]. For the sake of brevity, the abovementioned control strategies are not discussed in depth in this paper. For details, the reader is referred to cited literature and the recent review by Duan et al. [7].

At the forefront of HCCI combustion control efforts is the development of robust measurement techniques which provide control feedback data in the form of various combustion indicators. Typically, in-cylinder combustion can be quantified using the in-cylinder pressure signal, recorded with high resolution in terms of both amplitude and crank angle. The fundamental engine parameter derived from in-cylinder traces is cycle thermodynamic work and indicated mean effective pressure (IMEP). More detailed pressure analysis consists of first or second-law methods to derive the HRR functions in the crank angle (CA) domain.

The common belief is that measurement of in-cylinder pressure is the most accurate reference for combustion control. However, this method is very prone to systematic errors from the measurement setup or simplifying assumptions. For instance, Maurya and Agarwal [15] demonstrated that under typical conditions, a single crank angle degree (CAD) shift of the pressure curve - a triggering resolution used by many researchers - introduces a 12% error in IMEP determination. Considering the accuracy of the pressure sensor itself and the number of additional constants (compression ratio), variables and signal transformations, the error of peak HRR (HRR_{max}) determination is typically at least 8% [15]. Additionally, in-cylinder pressure sensors are expensive and have a short service life due to the harsh operating conditions [16].

Measurement of vibration and acoustic emissions are well-proven methods of providing signals which carry complete diagnostic information on machine conditions. Vibration sensors have been used to monitor engine condition and failures in marine and aviation applications [17]. For brevity, the exact measurement techniques and data analysis methods for condition-based maintenance using vibration monitoring will not be discussed here. The reader is referred to the review by Delvecchio et al. [18]. Vibration sensors are widely used in automotive applications to detect knocking combustion in spark ignition (SI) engines [19].

Vibroacoustic methods go beyond engine mechanical condition monitoring and abnormal combustion detection applications. The ultimate aims of numerous research studies include indirect in-cylinder pressure estimation and determination of combustion parameters. The critical condition for the robustness of vibration-to-combustion methods is the presence of individual signal features that differentiate with in-cylinder pressure and are not overlapped by other engine events. Lee et al. [20] applied continuous wavelet transform (CWT) to identify the combustion-induced frequency of CI engine-block acceleration. The authors found that combustion-borne vibrations cover the frequency range from 0.3 to 1.5 kHz, and this bandwidth is distinctive from the mechanical-induced vibrations. The work further compared the integral of the CWT coefficient in the selected band with HRR_{max} for different speeds and loads. A clear correlation was found, but the scattering of experimental data prevented accurate HRR_{max} determination. Zhao et al. [21] performed an S-transform (a generalisation of the short-time Fourier transform) on the vibration velocity data of CI engines, and identified similar combustion-induced frequencies. The authors introduced a model to filter inertia force components that overlapped combustion signals, striving to increase the accuracy of combustion parameters estimation. Yang and Yong [22] used the Fourier decomposition method to extract combustion components in the engine-head acceleration signal. Isolated Fourier intrinsic band functions were reassembled to yield solely combustion-induced vibration signals.

Importantly, Schaberg et al. [23] demonstrated a clear coupling between a CI enginés high PRR and the enginés acceleration signal amplitudes. The authors further focused on identifying sources of engine vibration, rather than using vibration signals to determine combustion parameters. The latter was followed up by Chiatti et al. [24], who identified characteristic points on the CI engine acceleration signal wave in which angular locations were correlated with characteristic points of the mass fraction burned (MFB) curve. The experiments, performed at different operating conditions, consistently showed good agreement between pressure-derived and vibration-derived combustion timing data. Furthermore, Yang and Yong [22], using the previously mentioned decomposition approach, were able to couple characteristic points on the vibration wave with locations of combustion onset, maximum PRR and peak pressure. All values were predicted with a maximum $\pm$ 0.9 CAD error.

The full reconstruction of in-cylinder pressure curves based on vibration signals has been deeply researched, with potential applications in mind. Most of the physics-based approaches use frequency response functions to identify common frequency components in vibration signals and pressure waves. Having estimated the transfer function, so-called inverse filtering is applied to reconstruct the pressure wave [25]. The pressure trace is assembled using a linear combination of vibration signal components, taken over a range of different frequencies. Notably, both engine-block acceleration and acoustic emission have been used successfully as input data [26,27]. However, it is important to note that accurate reconstruction of in-cylinder pressure at different engine speeds and loads requires the determination of a frequency response function specific to the given operating condition.

Signal-conditioning methods, designed to improve the robustness of the transfer function, include time domain filtering and cepstral analysis [26]. Antoni et al. [28,29] treated nonstationary vibration signals as a series of stationary events; the approach was called ‘cyclostationarity’. A periodically varying inverse filter, equivalent to 17 parallel invariant filters, was adopted to reconstruct the pressure trace. Zurita et al. [30] applied multivariate data analysis using partial least squares regression to reconstruct in-cylinder pressure during combustion. This method turned out to be more robust than cepstral analysis and pressure reconstruction using the fixed transfer function. However, the method involves three structurally different models to fit the data in different parts of the engine operating envelope. This reveals that the approach missed capturing the governing physics behind the modelling.

Black-box models have gained popularity recently, because computing capabilities are no longer a bottleneck for the application of complex numerical methods. Peña and Zurita [31] applied the artificial neural network (ANN) method to reconstruct in-cylinder pressure using multi-cylinder engine-block acceleration data. The vibration signals were time-windowed and filtered to diminish the effects of noise and other engine events. An accurate pressure reconstruction from vibration

Table 1
Summary of state of the art in vibroacoustic combustion estimation. The merits of the present study are included in the last row for comparison. Note that error definitions differ between studies.

Reference	Engine type	Operating conditions	Vibration sensor	Analytical approach	Combustion parameter estimation error, remarks
Azzoni (1997) [41]	SI, 4-cylinder, 1300 cm^3	3100–5000 rpm; free acceleration	Accelerometer	Determination of frequency response function, inverse filtering	Peak pressure: 4% (mean error)
Antoni et al. (2002) [29]	CI, 4-cylinder, 1905 cm^3	900 rpm	Accelerometer	Inverse filtering with periodically variable filters	–
Zurita et al. (2004) [30]	CI, 6-cylinder, 11000 cm^3	800–2000; 10%-100% of full load	Accelerometer PCB 353 M15, 1–10000 Hz	Multivariate data analysis for peak pressure prediction and partial least squares model for pressure reconstruction	Peak pressure: 5% @ 800 rpm, 39% @ 2000 rpm (mean error)
Peña and Zurita (2005) [31]	CI, 1-cylinder, 522 cm^3	800–2000 rpm; 10%-100% of full load	Accelerometer PCB 353 M15, 1–10000 Hz	Pressure reconstruction with GRNN model	Peak pressure: 1% (difference in STD)
Johnsson (2006) [33]	CI, 6-cylinder 11000 cm^3	800–2000 rpm; 10% −90% of full load	Accelerometer PCB 353 M15, 1–10000 Hz	RBF-ANN, input data: Fourier transforms of acceleration and crankshaft speed	Peak pressure: 3.4% (RMS error), location of peak pressure: 6 CAD (RMS error), PRR: 0.26MPA/CAD (RMS error)
Chauvin et al. (2008) [37]	HCCI, 4-cylinder, light-duty	1000–1500; 0.1–0.6 MPa(IMEP)	Acceleration-type knock sensor	Gaussian fit to instantaneous vibration energy, 1.5–3 kHz	CA50: approx. 5 CAD (mean error, systematic)
Massey et al. (2009) [42]	HCCI, 1-cylinder, 517 cm^3	1800 rpm, fixed low load	Accelerometer PCB HT356B21, 2–10000 Hz	Instantaneous specific kinetic energy, 1–4 kHz	CA50: 1.7 CAD (mean error on single stable operating point); accuracy deteriorated to ± 4 CAD at delayed combustion
Cheng et al. (2012) [36]	HCCI, 2-cylinder; 1630 cm^3	1200–1600 rpm	Velocity sensor GST CS-YD-005, 4–4000 Hz	Time domain, the first bent-point on velocity wave	SOC: 2.85 CAD (mean error, systematic)
Bizon et al. (2013) [43]	CI, 3-cylinder, 1028 cm^3	1800–3400 rpm; idle run	Accelerometer, up to 1.5 kHz	RBF-ANN	Peak pressure: 3.9% (RMS error), CA50: 1.6 CAD (RMS error)
Lee et al. (2015) [20]	CI, 4-cylinder, 1600 cm^3	1250–2000 rpm; 0.4–0.8 MPa (BMEP)	Accelerometer Kistler 8728A, 2–10000 Hz	CWT, cumulative value between 0.3 and 1.5 KHz	Peak HRR: 35% (max error), $R^2 = 0.892$
Grajales et al. (2016) [44]	SI, 1-cylinder, 143 cm^3 and SI, 4-cylinder, 2000 cm^3		Accelerometer	Polynomial regression, pressure calculated based on selected points on acceleration wave	Pressure values at selected points: 20% (RMS error for 1-cylinder engine), 28% (RMS error for 4-cylinder engine)
Chiatti et al. (2017) [24]	CI, 3-cylinder, 1028 cm3	1600–3600 rpm; 0.24–0.62 MPa (BMEP)	Accelerometer Endevco 7240C, max. 5000 Hz	Time domain, zero-crossing and bent points on acceleration wave	Start of combustion: 1.38 CAD (mean absolute error), MFB50: 1.32 CAD (mean absolute error), MFB95: 1.29 CAD (mean absolute error)
Zhao et al. (2017) [21]	CI, 1-cylinder, 815 cm^3	800–1400 rpm; 0.15–0.77 MPa (BMEP)	Velocity sensor GST CS-YD-005, 4–4000 Hz	Empirical mode decomposition, zero-crossing and bent points on velocity wave	Start of combustion: 1.1 CAD (max error), location of peak pressure: 0.8 CAD (max error)
Trimby et al. (2017) [34]	SI, 3-cylinder, 1125 cm^3	1000–2000 rpm; 0.11–0.34 MPa (BMEP)	Acceleration-type knock sensor	ANN	Complete pressure curve: 4.3% (RMS error)
Ji et al. (2018) [45]	CI, 12-cylinder, 71450 cm^3	1200 rpm, 0.2–1.4 MPa (BMEP)	Accelerometer GST CA-YD-102, 0.5–10000 Hz	S-transform	Peak pressure: 4.9% (mean error), PRR: 8% (mean error)
Han et al. (2018) [46]	CI, 4-cylinder, 2000 cm^3	1200–3000 rpm, 0.38–1.13 MPa (BMEP)	Accelerometer	Recursive estimation algorithm based on Kalman filter	Peak pressure: 4.5% (mean error), location of peak pressure: 1.9 CAD (mean error)
Ji et al. (2021) [40]	CI, 12-cylinder, 71450 cm^3	1200–1500 rpm, 0.14–1.1 MPa (IMEP)	Accelerometer GST CA-YD-102, 0.5–10000 Hz	Time domain, the first-bent point and zero-crossing point on acceleration wave	SOC: 2 CAD (max error); location of PRR: 1.5 CAD (max error)
Yang and Yong (2022) [22]	CI, 1-cylinder, 815 cm^3	800–1400 rpm; 0.15–0.77 MPa (BMEP)	Accelerometer GST CA-YD-102, 0.5–10000 Hz	Fourier decomposition method, zero-crossing and bent-points on acceleration wave	Start of combustion: 0.9 CAD (max error), location of peak PRR: 0.7 CAD (max error), location of peak pressure: 0.9 CAD (max error)
Nguyen et al. (2022) [39]	HCCI, 1-cylinder, 499 cm^3	900–2300 rpm; 0.16–0.45 MPa (IMEP)	Accelerometer PCB ICP M338A34, 0.7–3000 Hz	ANN (RBF, GRN)	Complete pressure curve: 0.19 MPa (RMS error); peak pressure: 0.08 MPa (RMS error); peak pressure location: 4.5 CAD (RMS error)
This work	HCCI, 1-cylinder, 499 cm^3	900–2300 rpm; 0.18–0.53 MPa (gross IMEP)	Accelerometer PCB ICP M338A34, 0.7–3000 Hz	Time domain, the first maximum point on acceleration wave	Location of peak HRR: 0.62 CAD (mean absolute error); peak HRR: 21% (mean absolute error)

data was obtained using the generalised regression ANN architecture. The research covered a wide range of engine loads and variable rotational speeds. Using radial basis function architecture, Bizon et al. [32] also proved high accuracy of CI engine combustion pressure reconstruction in the CA window ± 30 CAD around the piston top dead centre (TDC). The authors demonstrated the robustness of the ANN model, verifying it under variable operating conditions and fuels. Increasing rotational speeds from 1000 rpm to 2000 rpm decreased prediction accuracy. The authors also estimated other pressure-derived combustion parameters, apart from pressure waves. For example, 50% MFB location (CA50) was estimated with accuracy of better than a single CAD. Notably, the predicted CA50 value was always delayed with respect to the pressure-derived one. Johnsson [33], used the Fourier transforms from vibration acceleration and crankshaft speed signals as input data to the radial basis function (RBF) network. This was substantiated by the finding that the crankshaft speed fluctuations respond better to low-frequency pressure components, whereas vibrations performed better for higher frequency content. Consequently, the use of a two-channel algorithm improved the models robustness. Based on similar assumptions, Trimby et al. [34] demonstrated high accuracy of time-delay feedforward ANN for pressure reconstruction from either acceleration signal or crankshaft speed.

The above summary captures the state of the art in combustion monitoring techniques from the perspective of conventional engine concepts. It should be noted that the common feature of the discussed vibration-based combustion estimation methods is the lack of predictability. In other words, these methods for CI engines are strictly data-driven and hence valid only for specific test objects, with accuracy secured within the model calibration space.

Turning to LTC, volumetric combustion yields a high PRR which generates a more distinctive vibration amplitude [35]. Despite this advantageous feature, successful attempts to describe combustion using the vibroacoustic spectrum in HCCI are scarce, compared to the abundant CI applications. Cheng et al. [36] investigated the feasibility of identifying the onset of HCCI combustion by using a vibration velocity signal and applying high-fidelity finite element method simulations. The authors concluded that the position of the first turning point in the vibration wave, generated by combustion, correlates well with the start of combustion. Experimental verification under variable engine operating conditions proved only ± 0.5 CAD error in the estimation of the start of combustion. Applying a similar premise, Chauvin et al. [37] used a knock sensor signal to determine CA50 in a diesel engine operated in HCCI mode. The approach involved a Gaussian function fitted to the knock energy curve to smooth the signal harmonics. The peak value of the function was interpreted as the CA50. The method was demonstrated in transient control, with vibration-based feedback data embedded in the engine controller [38]. The absolute-level accuracy of the CA50 determination was not analysed and the method was considered valid by the successful control application. Recently, Nguyen et al. [39] tested HCCI in-cylinder pressure reconstruction from vibration acceleration using ANN. The initial tests resulted in deteriorating accuracy outside the neural network training matrix. Changing the model to general regression improved the fit, allowing the conclusion that the vibration signal carries sufficient information to estimate combustion parameters independently on the engine platform or combustion concept.

2. Motivation and contribution of the present study

Table 1 summarises the state of the art in vibroacoustic combustion characterisation, discussed in the introduction. One can immediately notice that the technology is relatively well-established for conventional combustion concepts. For compression ignition (CI) engines, all of the works included in Table 1 considered a purely data-driven approach to reproduce the combustion indicators either directly or indirectly (through in-cylinder pressure reconstruction). In this respect, contemporary black-box methods are capable to reproduce relevant combustion indicators (CA50 or CA of peak PRR) with accuracy sufficient for closed-loop combustion control applications, i.e. with a mean error below 1 CAD [21,22] For multi-cylinder CI and SI engines the accuracy deteriorates slightly with corresponding errors not exceeding 1.5 CA [24,40].

However, the phenomenological complexity of the combustion and the nonlinearities associated with it render purely data-driven vibroacoustic combustion estimation approaches, commonly proposed for CI engines, ineffective for LTC applications (refer to Table 1). Limited works that proposed such an approach for HCCI, using a full operational envelope test matrix, were bearly able to predict the combustion onset with errors below 4 CA [37,39]. Notably, peak HRR or PRR values that are relevant for establishing operational limits are extremely difficult to capture in HCCI due to their rapid and random nature. For vibration-based methods, the state-of-the-art accuracy in this respect does not exceed 50% [39].

Prospective HCCI technology provides new opportunities for vibroacoustic combustion estimation, building on the more transparent signal pattern. However, the extraction of the relevant combustion data, to meet the accuracy and robustness targets imposed by closed-loop control, needs a new approach that increasingly relays on combustion phenomenology. The present study, through a fundamental analysis of the combustion-vibration phenomena in the HCCI regime, develops new correlations for governing combustion control parameters. The correlations are successfully validated on a state-of-the-art single-cylinder research engine on a broad range of HCCI operating points. According to the benchmark in Table 1, the new method demonstrates superior performance over approaches proposed earlier. The combustion timing mean estimation error is reduced to 0.67 CA (peak HRR location) and the corresponding estimation error for the peak HRR value is cut down by half compared to state-of-the-art ANN-based methods.

Table 2
Technical data of the research engine.

Parameter	Value
Operating mode	four-stroke, NVO
Swept volume	498.5 cm^3
Cylinder bore	84 mm
Piston stroke	90 mm
Geometric compression ratio	11.5:1
Number of valves	2
Intake cam profile	9.4 mm, 235 CAD
Intake cam lift	2.4…9.4 mm
Exhaust cam profile	9.2 mm, 235 CAD
Exhaust cam lift	2.2…9.2 mm
NVO duration	variable (157–173 CAD)
Fuel injector	Bosch HDEV, direct, single-stream, swirl-type, electromagnetic
Fuel	pump-grade gasoline
Fuel pressure	9.5 MPa
Air-path	naturally aspirated with ambient intake temperature

3. Experimental methods and procedures

3.1. Research engine and dynamometer test stand

Experimental data in this study come from a single-cylinder research engine test bench at Lublin University of Technology, Poland. Fuelled by gasoline, the engine achieves HCCI by utilising variable valve actuation (VVA) and employing NVO strategy. The cylinder volume and compression ratio are typical of car SI engines. Fuel is delivered directly to the cylinder using an electromagnetic injector. The additional energy for gasoline auto-ignition is provided only by the internally recirculated exhaust. Table 2 gives the relevant data of the research engine.

A brief description of the engine test bench mechanical design features is given to assist interpretation of the results. These features are responsible for additional excitations and influence the vibration transfer path. Firstly, the single-cylinder research engine is based on a floor-standing, cast-iron crankcase, which houses a crankshaft and inertia balancing shafts. The liquid-cooled cylinder and engine head are located on the mounting plate, which covers the top of the crankcase. The design of the engine head enables smooth adjustment of valve timing and valve lift, the most important functions of the mechanical system enabling internal EGR via NVO.

The design of the research engine head is different from typical automotive production engines, which affects the vibration spectrum. A cross-section of the engine is depicted in Fig. 1. Note that the two symmetrical camshafts (1 and 1′) are propelled by a toothed belt and equipped with mechanisms which enable their rotation in relation to the gear's position. This function serves as a valve timing adjuster. The valve lift adjustment system is hydraulic. The intake and exhaust valves are not actuated directly by the respective cams, but by a set of three interconnected hydraulic cylinders. The first of these cylinders (4) is a cam-driven hydraulic pump. The second (6) acts as a hydraulic accumulator, which is filled with oil until the piston reaches an adjustable bumper (9). The third cylinder (5) opens the valve (10) when the piston position is fixed by the bumper. This VVA mechanism modifies the valve lift profile in such a way as if the cam profile did not change, and only

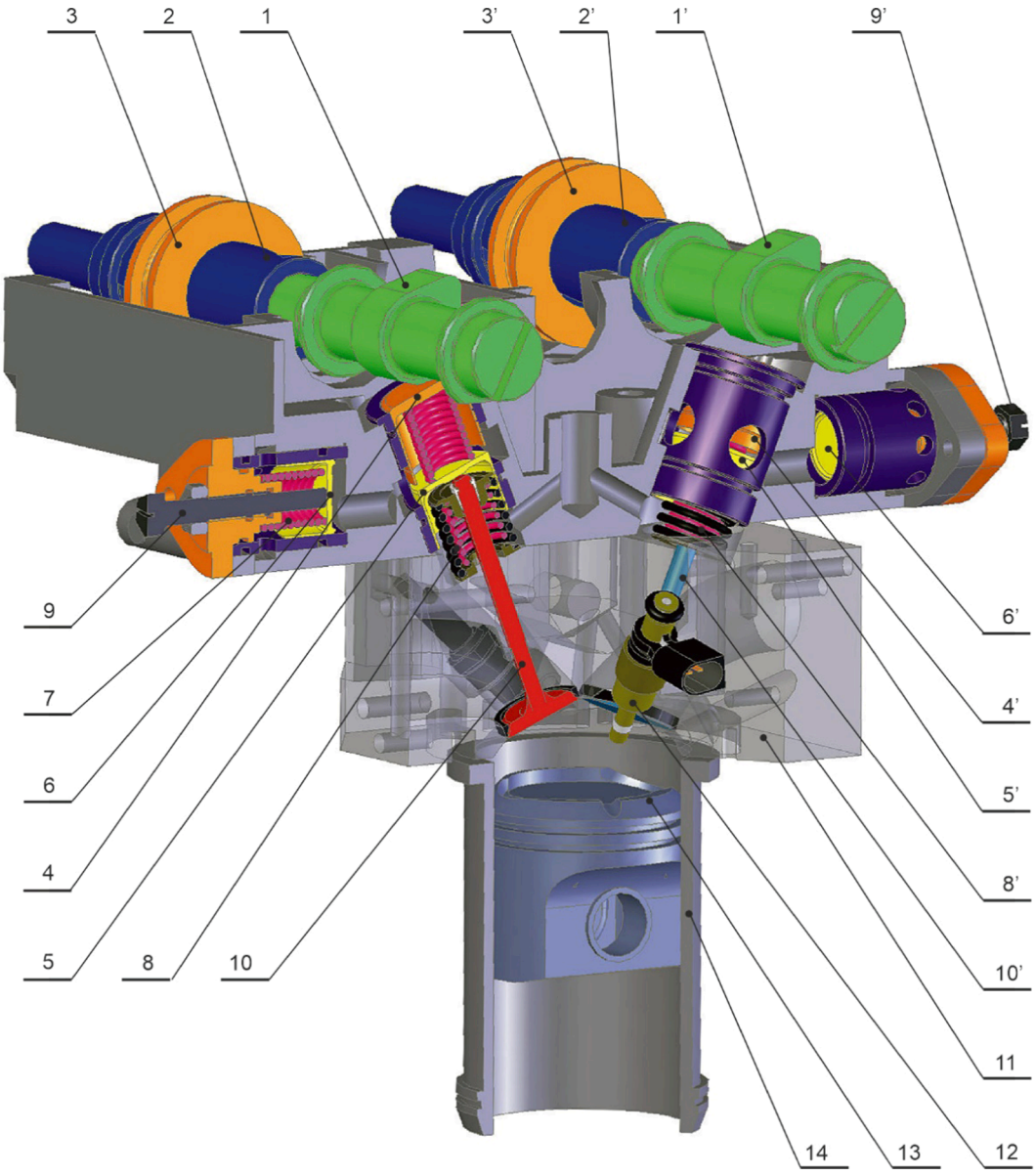

Fig. 1. Research engine's cross-section [47]: 1 – camshaft, 2 – drive shaft, 3 – sliding sleeve, 4 – cam piston, 5 – valve piston, 6 – hydraulic accumulator piston, 7 – hydraulic accumulator spring, 8 – valve springs, 9 – valve lift regulating screw, 10 – valve, 11 – engine head, 12 – fuel injector, 13 – piston, 14 – cylinder liner.

the valve clearance is variable, but to a very large extent compared with a typical engine.

The valve lift adjusters produce much more vibration than a typical engine head, but their footprint is separable from the combustion-induced vibration signal. This topic of separation is addressed in the results discussion section.

The engine is coupled to a DC dynamometer, which is driven by controllable six-pulse rectifier. The dynamometer control system is operated in the mode which stabilises rotational speed, regardless of engine torque. The test stand is equipped with thermal conditioning systems for fuel, oil and cooling liquid, plus all the automation enabling full control of engine operating conditions. The test stand is also equipped with all necessary instrumentation to acquire thermodynamic conditions of all media: fuel, intake air, exhaust, oil and cooling liquid. The air–fuel ratio can be accurately determined by thermally conditioned air- and fuel-flow measurement lines. Additionally, a wide-band lambda probe provides a reference lambda value for control purposes.

Table 3
Data of the pressure transducer.

Manufacturer	AVL	
Type	GH12D	
Sensitivity	156	pC/MPa
Measurement range	0…25	MPa
Accuracy	± 0.5…2%*	FSO**
Linearity	± 0.3%	FSO**
Natural frequency	115	kHz
Acceleration sensitivity	< 0.1	kPa/g
Cyclic temperature drift	< 0.05	MPa
IMEP*** stability	< 3%	

*) Depending on temperature: 20…400 °C <± 2%, 200…300 °C <± 0,5%.
**) FSO – full-scale output.
***) IMEP – indicated mean effective pressure.

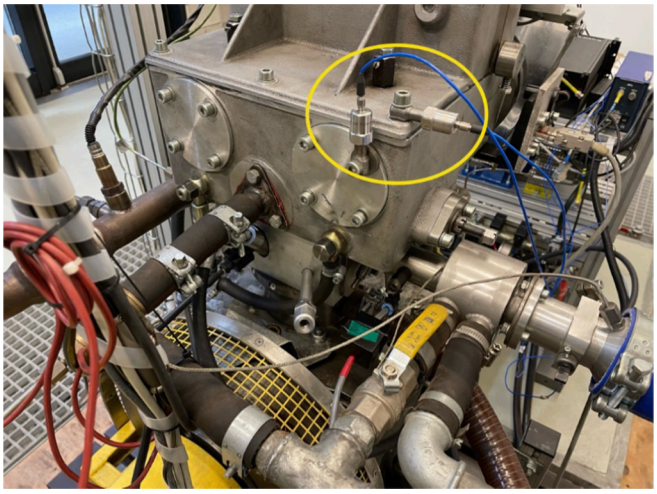

Fig. 2. Location of accelerometers on the engine head.

Table 4
Data of the accelerometers.

Manufacturer	PCB PIEZOTRONICS	
Type	PCB ICP M338A34	
Sensitivity	108.9	mV/(m/s^2)
Measurement range	± 4905	m/s^2
Frequency range (±5%)	1…2000	Hz
Frequency range (±10%)	0.7…3000	Hz
Resonance frequency	>12	kHz
Wideband sensitivity	± 0.2	m/s^2
Linearity	± 1	%
Cross sensitivity	<5	%
Impact resistance	± 19,620	m/s^2 pk
Operating temperature	–54…121	°C
Temperature coefficient	< 0.09	%/°C
Stress sensitivity	< 0.05	m/s^2/με)

3.2. Pressure and vibration measurement

The study focuses on two measurement signals. First, in-cylinder pressure is used as a basis for detailed thermodynamic analysis of combustion. The second signal is the vibration acceleration, explored for its potential to extract combustion control information correlating with the above pressure-based reference. These two measurement methods are discussed in more detail below.

In-cylinder pressure is measured with the use of a miniature piezoelectric transducer by AVL. Table 3 lists the sensoŕs characteristics. The pressure measurement diaphragm is uncooled and directly exposed to the combustion chamber in order to avoid signal delays and dumping. The charge signal is converted into voltage with a dedicated charge amplifier.

Two accelerometers are used to provide vibration data. One is mounted vertically, parallel to the cylinder axis; the other is positioned horizontally, parallel to the crankshaft and perpendicular to the cylinder liner. Fig. 2 shows these locations. Table 4 provides the accelerometeŕs specifications.

The pressure and vibration voltage signals are synchronically recorded using National Instrumentś PXI 6071E analogue–digital (A/D) measurement card built into the PXI-8119 laboratory computer. The resolution of the A/D converter is 12-bit, whereas the maximum sampling frequency is 1.25 MHz. The A/D converter is triggered by a crankshaft optical encoder with a constant resolution of 0.1 CAD. Note that the CA domain is used to provide synchronisation with cylinder volume and further thermodynamic analysis. The synchronisation is secured by a dedicated internal counter for both measurement channels. The data were recorded for 100 consecutive engine cycles at each steady-state operating point of the test matrix.

3.3. Data analysis procedures

3.3.1. Cycle-individual thermodynamic analysis

In-cylinder pressure is instrumental for detailed thermodynamic analysis. This is conducted according to well-established and thoroughly validated combustion engine research methods, adapted to the specific domain requirements of the corresponding vibroacoustic analysis. The recorded relative pressure traces for individual cycles were first low-pass filtered and pegged. To secure high accuracy for the pressure-derived indicators, the pegging used the fast (crank angle-based) absolute pressure signal from the intake port as a reference value to correct the in-cylinder pressure around the valve flow stagnation point.

The post-processed in-cylinder pressure is used directly to calculate the PRR and IMEP. PRR is an important parameter determining mechanical stress and is considered a primary excitation for combustion-induced vibration [22]. The CA-dependent PRR function and its peak value (PRR_{max}) have been calculated directly as a discrete derivative of in-cylinder pressure, smoothed over a single CA measurement interval. IMEP represents the cycle's ability to perform work and is calculated as a ratio of the cycle's thermodynamic work, divided by the cylinder's swept volume (V_s), using the following formula:

$$\mathrm{IMEP} = \frac{1}{V_s}\oint p\mathrm{d}V \tag{1}$$

where p and V are instantaneous in-cylinder pressure and volume. Note that the IMEP definition used in this study is gross and calculated for one crank revolution, consisting of compression, combustion and expansion. This is to exclude the thermodynamic processes during NVO from the analysis. The cycle-individual IMEP was further cycle-averaged to provide reference values characterising the operating point.

Note that typical thermodynamic analysis beyond the IMEP is conducted on the cycle-averaged signal. However, this studýs need to accurately analyse the combustion in-cycle requires the cycle-individual cylinder trapped mass and composition as an input in order to determine the instantaneous ratio of specific heats in Eq. (2). To this end, thermodynamic analysis was coupled with an in-house zero-dimensional flow model, which calculated flows having in-cylinder pressure and the intake/exhaust port pressures/temperatures as boundary conditions. For brevity, the model is not discussed here, but the reader seeking more details is referred to the work by Hunicz [47].

The following combustion analysis is based on the first law of thermodynamics. The apparent heat release rate is calculated using the following formula:

$$\mathrm{HRR} = \frac{\gamma}{\gamma-1}p\bullet\Delta V + \frac{1}{\gamma-1}V\hat{\mathrm{A}}\cdot\Delta p \tag{2}$$

where the discrete derivatives of volume (ΔV) and pressure (Δp) were calculated every 0.1 CAD. The ratio of specific heats (γ) is calculated from the instantaneous temperature and composition of the in-cylinder mixture, involving the mentioned variations in the gas exchange process and the species balance during combustion. The bulk gas temperature is calculated at every CA, using the equation of state, with consideration of the effect of mixture composition on the gas constant. The detailed description of the algorithm for determination of HRR and MFB can be found in [48]. The apparent HRR includes heat of fuel combustion and heat transfer through combustion chamber walls. As combustion-borne engine vibrations are a combined effect of both phenomena, the apparent HRR was not further corrected towards gross values. The analysis is thus free from arbitrary assumptions imposed by the heat-loss model, increasing the accuracy of the combustion indicators to be correlated with vibration data. One needs to note that all the correlations discussed further in this study refer to the apparent combustion parameters.

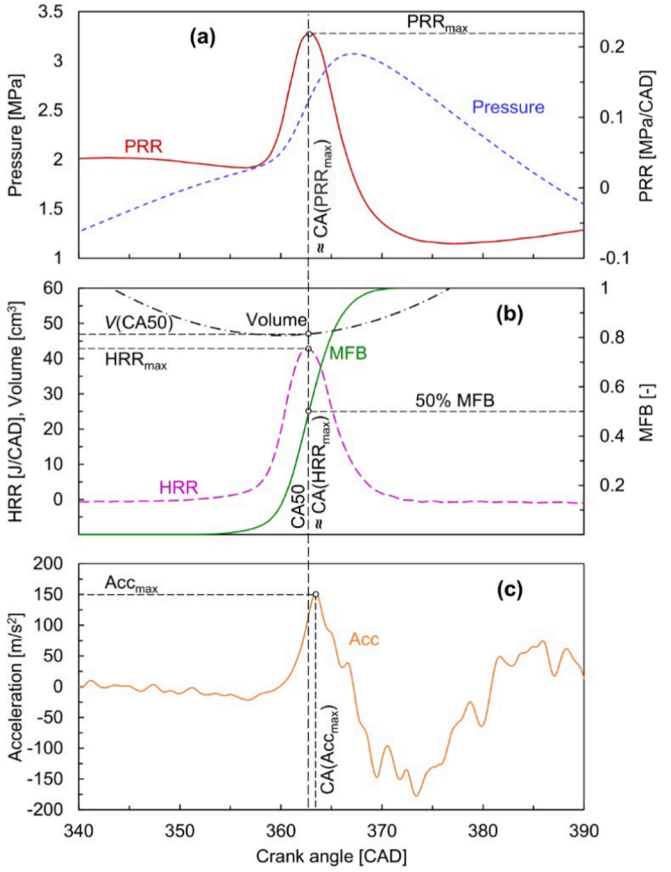

Fig. 3. Exemplary in-cylinder pressure with calculated PRR (a), calculated HRR and MFB functions, cylinder volume (b) and acceleration signal (c). The definitions of analysed combustion and vibration parameters are also introduced in the figure.

The HRR curves carry all the information required for the implementation of closed-loop LTC control. Integration of HRR and proper scaling yields the fuel MFB function, from which characteristic combustion stages, expressed by percentages of MFB, can be read. Fig. 3 depicts the above-mentioned definitions, along with key combustion timing parameters. Notably, the presented data comes from the research results analysed in this study.

Previous studies attempted to correlate engine vibration with various parameters, characterising the HRR synthetically. The present work approaches the problem more fundamentally. The crank angle of HRR_{max} is a direct and ultimately one of the most important combustion timing indicators for HCCI control. This parameter directly determines the thermodynamic efficiency and combustion harshness, which is one of the main limitations of high-load HCCI operation [49]. Thus, this study extracts angular locations of the peak HRR from the HRR curves, and subjects them to detailed statistical analysis.

3.3.2. Vibroacoustic and statistical analysis methods

Vibration data are represented by crank-angle-associated acceleration values. These signals were, similarly to in-cylinder pressure, elaborated for each cycle separately. Before in-depth analysis, the cycle-individual vibration acceleration signal was subjected to low-pass filtering, in order to remove white noise. In a previous study, it was determined that vibrations in the direction of the cylinder axis contain more combustion data than in perpendicular directions [50]. Therefore, only the vertical acceleration signal was further analysed.

A wavelet analysis was performed to identify the signal's frequency spectrum. The reader should refer to [51] for details of this technique. It is sufficient here to mention that wavelet analysis provides a spectral–temporal picture of the time series, showing variability of dominant frequency components in time. This is particularly useful for analysing intermittent phenomena, like combustion in reciprocating engines [52,53]. A complex, 6-order Morlet wavelet is used as a mother wavelet, as it provides a good balance between time and frequency. This wavelet analysis, along with standard frequency response analysis tools like fast Fourier transform (FFT) [54], support the discussion of the results.

The peak acceleration, HRR_{max} and their respective angular locations (Fig. 3), along with the instantaneous IMEP, are selected in search of correlations, and analysed statistically. Here, the standard deviation (STD) and the coefficient of variation (CoV) are the basic measures of cycle-by-cycle variability for all analysed parameters. More advanced correlation methods in this study involve multivariate data analysis [55], used to obtain accurate models reconstructing in-cylinder pressure parameters from vibration signals. Regression techniques are applied to investigate relationships among variables and to reduce the number of predictors. The goal is to identify the smallest possible set of components that provide the greatest predictive abilities.

3.4. Theoretical framework for determining HRR from vibration acceleration

Combustion-induced engine vibration can be considered vibrations of a stiff vessel, caused by rapid in-cylinder pressure gradients (Δp). The pressure gradient resulting from the heat release during combustion can be derived analytically from the first law of thermodynamics. The transfiguration of Eq. (2) yields:

$$\Delta p = \frac{1}{V}\left[\Delta Q(\gamma - 1) - \gamma \bullet p \bullet \Delta V\right] \tag{3}$$

Taking the assumption that combustion in HCCI is very rapid (as proven in Fig. 3) as a first-order simplification, the component of Eq. (3) associated with the change of volume (ΔV) during combustion can be omitted. Scaringe et al. [56] further demonstrated that the cumulative heat release can be considered linear for volumetric-type combustion. This was later verified for the NVO-HCCI combustion concept considered here, in another work by Hunicz et al. [49]. The linearity of the cumulative HRR is evident from Fig. 3b. Considering the above-mentioned argument, while combustion is properly positioned around TDC, the cylinder volume at $CA(HRR_{max})$ can be used in Eq. (3) to arrive at PRR_{max}:

$$PRR_{max} = \frac{HRR_{max}(\gamma - 1)}{V(CA(HRR_{max}))} \tag{4}$$

Note that the above assumption means that the HRR in HCCI is symmetrical before and after the CA50, and assumes that CA50 is equal to $CA(HRR_{max})$, as indicated in Fig. 3. This has been confirmed in Hunicz et. al [49], considering that we disregard the CA dependency of γ.

With PRR_{max} analytically correlated to HRR_{max}, the next linking step to vibration is theoretically straightforward. Both quantities are bonded with a structure transfer function in terms of amplitude-frequency and response delay. Theoretical methods to determine the transfer function for the given engine structure do exist [57], but require dedicated tests with a banger rig, and so are not suitable for control purposes. Instead, a data-driven approach, based on regression techniques described in Section 3.3.2, is adopted to correlate HRR_{max} with peak vibration acceleration in terms of both amplitude and timing.

3.5. Experimental conditions

The experiments were performed at selected points of a speed-load map of the naturally aspirated HCCI engine. At wide-open throttle, engine load was controlled by the mass of fuel, whereas VVA allowed the desired air–fuel ratio and internal EGR. Different fuel injection strategies were applied at different load points. At low load, where exhaust

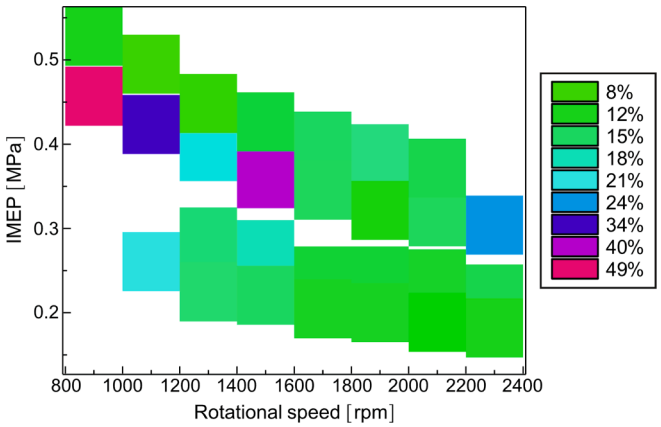

Fig. 4. Coefficient of variation (CoV) in HRR_{max}.

temperature is insufficient to enable auto-ignition, approximately 10% of fuel was injected during NVO exhaust recompression to utilize exothermal reforming. The remaining, main fuel value was injected during the intake stroke to create a premixed charge. At higher loads, the fuel dose was split into two equal parts, where the first injection was applied during NVO exhaust expansion (mixture cooling effect), while the remaining fuel was injected during the intake stroke. The air–fuel ratio was changing accordingly, from stoichiometric for high loads to lean mixture for low loads. As we are looking for a generic correlation, the control parameters setpoints are of secondary importance and so are not discussed in detail. The studýs experimental matrix was designed to explore different combustion timings, pressure rise rates and the combustion variability levels manifesting in an HCCI regime. Note that the engine was operated with acceptable levels of efficiency and emissions under all conditions. However, the optimisation of those indicators was not the explicit goal of the experimental campaign.

Fig. 4 depicts the speed/load envelope of this multi-dimensional calibration. To show the spectrum of different combustion conditions relevant to the goal of the present study, the map values depict CoV in HRR_{max}. Cycle-by-cycle variability under most conditions was kept within the limit of stable operation, which, by convention, is set at 4% CoV in IMEP [58]. The only exception was the point 900 rpm/0.45 MPa, where CoV in IMEP was 7%.

High combustion variability for intermediate engine-load and speed range 900–1500 rpm deserves comment. Combustion variability at this operating condition is associated with low enthalpy added to the mixture by NVO and its associated late combustion. One should note that unburned hydrocarbons from the late, incomplete combustion in the first cycle, are undergoing exothermal reactions and produce highly reactive species at NVO. These hot and reactive residuals are retained in the following cycle, promoting excessive combustion. This feedback loop between consecutive combustions in an NVO-enabled HCCI engine

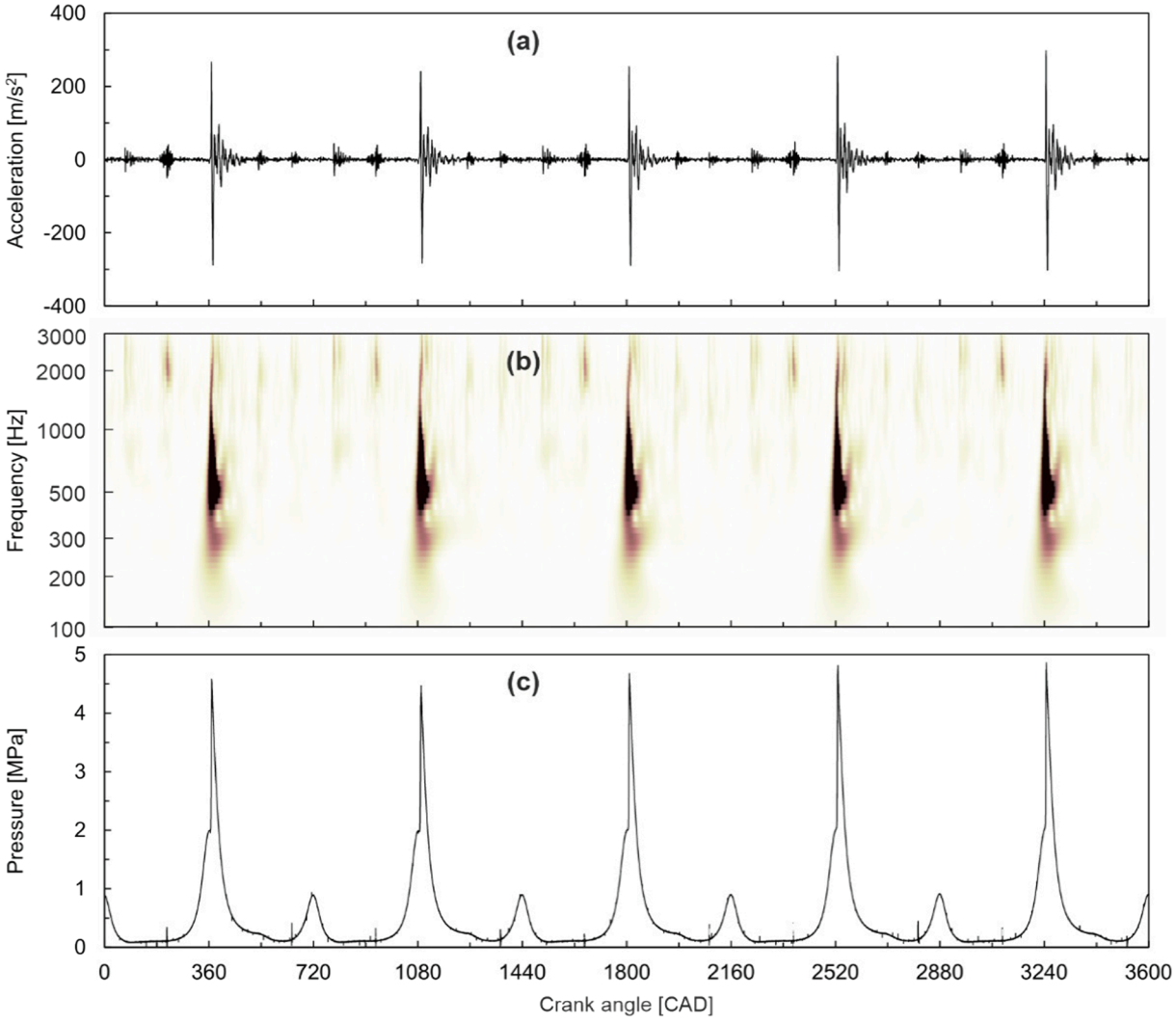

Fig. 5. Vibration signal (a), wavelet transform power density (b) and pressure signal (c) at $n = 917$ rpm and IMEP = 0.53 MPa.

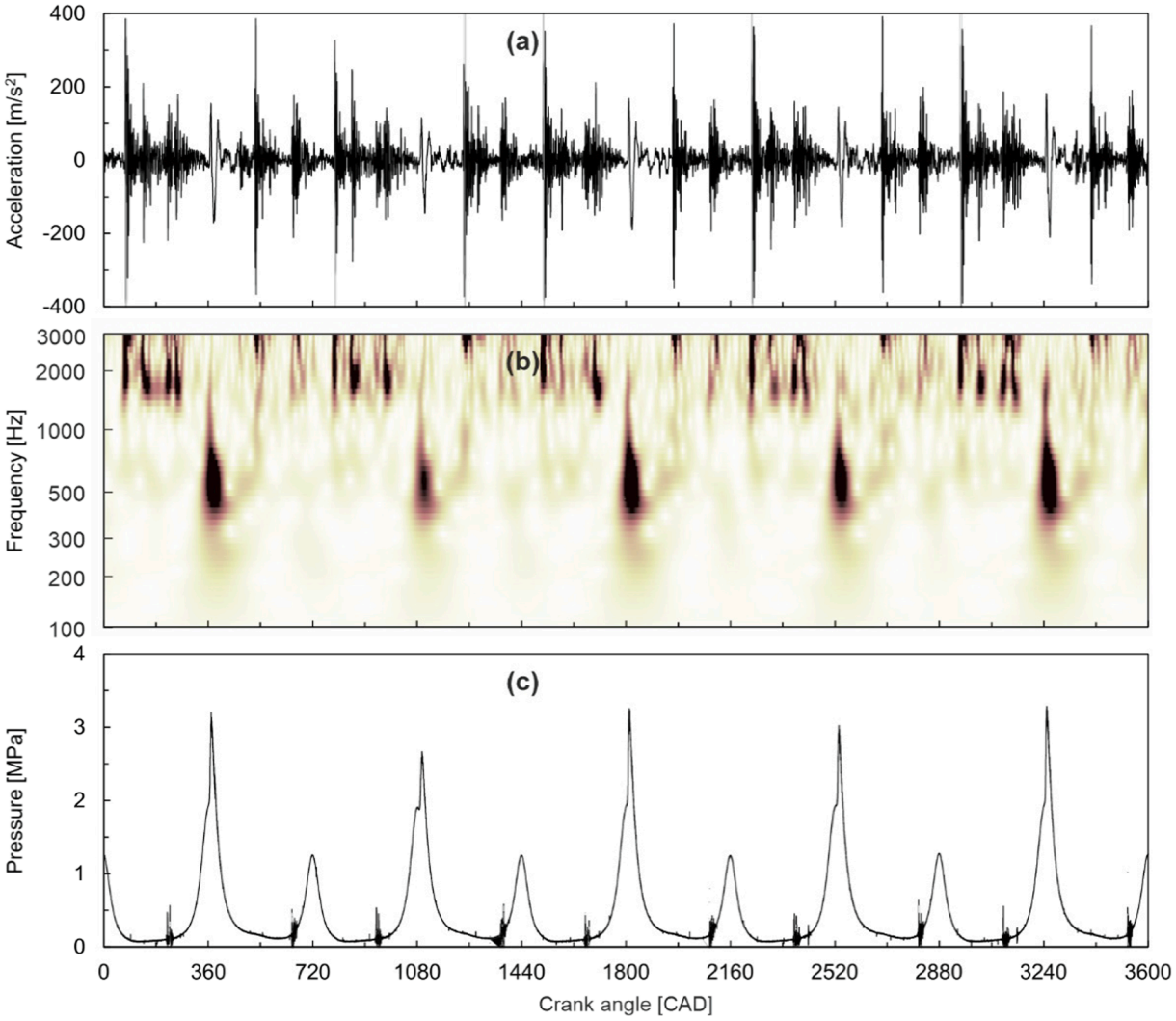

Fig. 6. Vibration signal (a), wavelet transform power density (b) and pressure signal (c) at $n = 2291$ rpm and IMEP = 0.22 MPa.

leads to cycle-to-cycle oscillations of auto-ignition timing and the total heat released during the main combustion cycle [59]. The large variations in HRR are symptoms of abnormal combustion. Nevertheless, these operating points are included in the test matrix to allow verification of the elaborated correlations under high cyclic variability.

4. Results

4.1. Vibration spectrum identification

First, we focus on selected points of the test matrix, demonstrating the specific features of the whole engine vibration spectrum. Two exemplary points of the test matrix are examined, denoted as high-load/low-speed and low-load/high-speed respectively. These represent the maximum achievable load in the HCCI mode (top left corner in Fig. 4); and the maximum speed point with low-load, respectively. Figs. 5 and 6 present five consecutive cycles of the in-cylinder pressure and vibration signal for these two operating points. Note that the crank angle is scaled to 0 at the gas exchange TDC. Consequently, combustion TDC in a four-stroke cycle is recurrently at 360 + 720 CAD.

Focusing on the high-load/low-speed operating point, it is evident in Fig. 5, that peak-load HCCI operation is limited by excessive in-cylinder pressure and PRR. Combustion is very rapid and peak in-cylinder pressures approaching 5 MPa are close to the mechanical stress limit of the research enginés head. Note that typical production engines tolerate only about half that value. It is noteworthy that combustion is very stable, as evident in Fig. 4, with CoV(HRR_{max}) = 11.9% and CoV(IMEP) as low as 1.4%. It is also worth noting that in HCCI engines, relatively high variability in heat release parameters does not translate into high IMEP fluctuations, because combustion is quick and takes place near TDC. This operating point is a good basis to discuss qualitatively the characteristics of both in-cylinder pressure and vibration spectrum in HCCI mode.

Aside from rapid PRR attributed to kinetically controlled and volumetric in nature combustion, the HCCI in-cylinder pressure signal exhibits a distinctive re-compression during the gas exchange phase (around 1 MPa peak at each 720 CA). This is attributed to NVÓs control mechanism in HCCI. NVO traps large amounts of hot internal recirculated exhaust gas in the cylinder, supporting gasoline auto-ignition around firing TDC.

The combustion events are clearly visible in the acceleration signal in Fig. 5, with the highest vibration amplitude around each consecutive firing TDC. Importantly, at NVO TDC, the vibration amplitudes, resulting from compression pressure and engine imbalance, are negligibly lower. It supports the validity of our initial assumption to disregard compression and the engine's inertial forces. The four lower-amplitude events clearly evident in the raw vibration signal between each combustion cycle, are attributed to the valvetrain. In sequence, they correspond to intake valve opening (IVO) at 83 CA; intake valve closing (IVC) at 213 CA; exhaust valve opening (EVO) at 527 CA; and exhaust valve

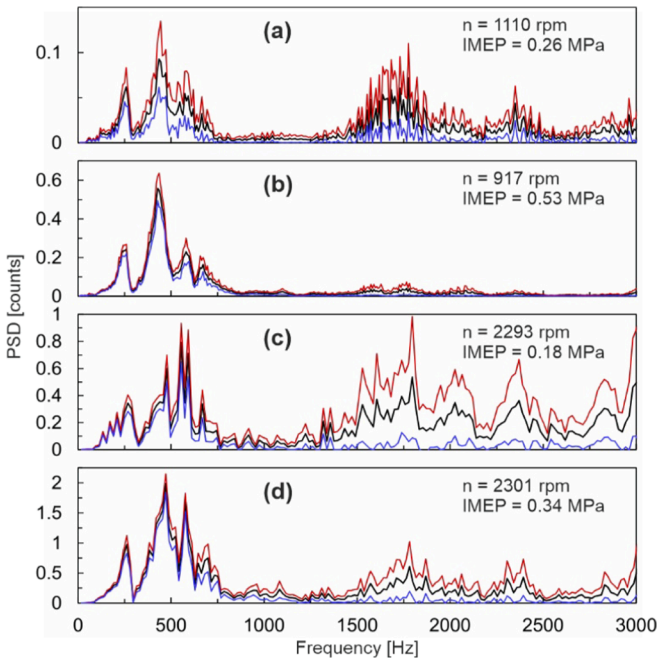

Fig. 7. PSD of vibration signal for selected engine speeds and loads. The black line is the cycle-averaged signal, while the red and blue lines indicate the mean ± STD cyclic-variability envelopes.

closing (EVC) at 646 CA. These valvetrain event locations refer to the first cycle in Fig. 5.

The valve and the combustion event do not coincide in terms of phase, and the wavelet power spectrum in Fig. 5 shows that they also have different frequencies. The dominating frequency during combustion is approximately 500 Hz, whereas valve events generate vibrations at around 2 kHz. Detailed analysis of the acceleration signal in the combustion window reveals that the first vibration peak coincides with the start of the rapid pressure rise rate associated with combustion. Intuitively, this peak is generated by energy release in the cylinder and the following wave is a result of free engine vibrations.

Fig. 6 shows that at higher rotational speed (2291 rpm) the valvetrain-induced vibrations are an order of magnitude stronger in terms of amplitude compared to the low engine-speed results in Fig. 5. However, the combustion-induced vibrations in Fig. 6 are halved, as overall energy provided by fuel is lower for this low-load operating point. Achieving high-load HCCI combustion at high engine-speeds is limited by gas flow restrictions.

Lower combustion-induced vibration amplitude, together with strong valve-induced vibration, make the signal more difficult to identify. However, it is significant that the peak wavelet power density for combustion in Fig. 6 is around the same 500 Hz frequency range as for the case in Fig. 5, and the valve events have also the same frequencies in both cases. Thus, the frequencies of both combustion and valve slapping appear to be independent of rotational speed and load.

To verify the above thesis, Fig. 7 shows the FFT-calculated power spectral density (PSD) functions for other distinctive operating points of the engine operating map. The calculations were performed for each cycle separately and cycle-averaged. Additionally, crank angle functions of STD show variability in terms of amplitude and frequency.

Fig. 7 shows that the combustion-induced vibration signal is clearly separated from other, mechanically induced, signals. Combustion-induced signal wavelengths cover the bandwidth between 100 Hz and 750 Hz. It is important that this bandwidth does not depend on engine speed nor load. Also, all the individual differences in PSD frequency/amplitude attributed to different combustion conditions, such as reaction rate, mixture temperature, etc., fall in this particular range. This

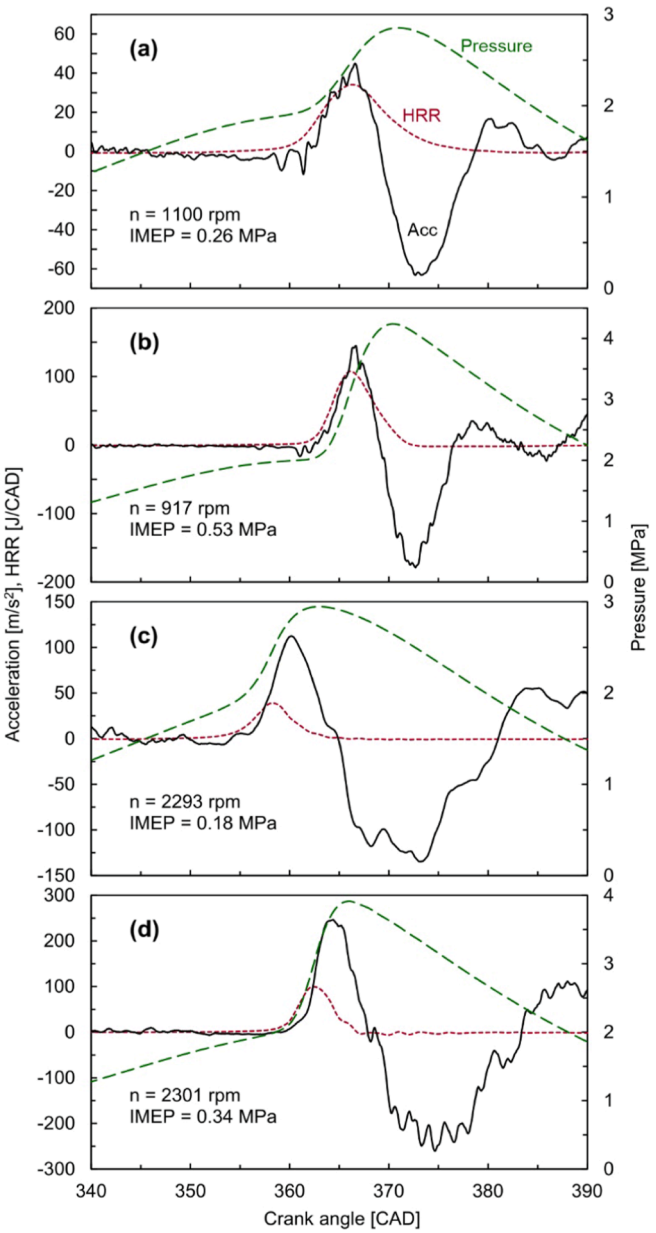

Fig. 8. Cycle-averaged in-cylinder pressure, HRR and vibration acceleration signals for selected HCCI operating points.

clear separation of crank angle/frequency domain between two major contributors of vibration in HCCI means no additional filtering is required to extract the combustion spectrum, assuming phase-windowing is applied.

4.2. Combustion-induced vibration vs. in-cylinder thermodynamic data

As mentioned, HCCI combustion is initiated around TDC firing and is spontaneous. Typical combustion duration in HCCI does not exceed 10 CA. Following the reasoning of the previous section, the focus of the combustion analysis window is the region between −20 CAD and 40 CAD after TDC. Fig. 8 gives this focused perspective of the selected operating points shown in Fig. 7. The cycle-averaged vibration acceleration signal is overlaid on the HRR resulting from the thermodynamic analysis of the in-cylinder pressure.

A comparison of acceleration and HRR amplitudes suggests that the amplitudes and locations of the first acceleration peak correlate with peak HRR and their locations. It is evident in Fig. 8a and 8b that there is

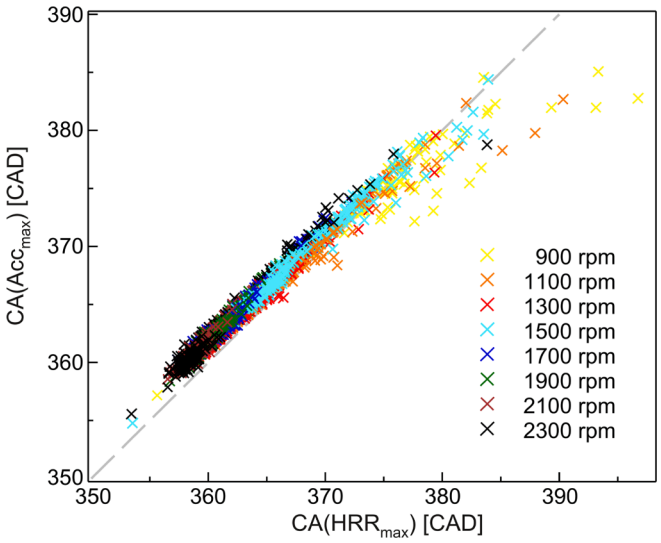

Fig. 9. CA(Acc$_{max}$) vs. CA(HRR$_{max}$) for individual cycles at all operating points.

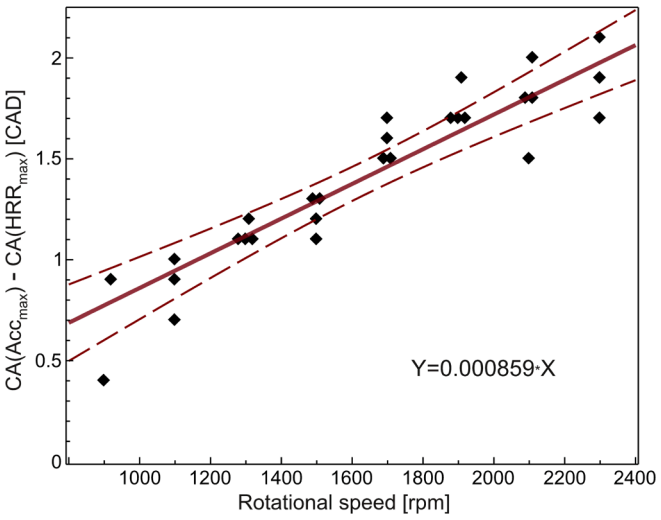

Fig. 10. The delta between CA(Acc$_{max}$) and CA(HRR$_{max}$) vs. rotational speed. Values are cycle-averaged and the median is used as the quantifier. The confidence intervals are calculated for all the cycles independently.

a good absolute-level agreement for low engine-speeds: 1 J/CAD in HRR$_{max}$ corresponds to approximately 1 m/s^2 in acceleration. But at high engine-speeds, the acceleration amplitudes are significantly higher than the HRR$_{max}$ values, and the vibration signal lags behind HRR. It takes less time for combustion to conclude at higher engine-speeds, but the vibration transfer path through the cylinder remains limited by the speed of sound, which is independent of engine speed.

The noticeable high-frequency component of the vibration signal is a result of cycle-to-cycle variability, revealing intermittent behaviour in terms of combustion phasing. Additionally, cyclic variability blurs the signal peaks. Finally, the nature and magnitude of cyclic variability can differ, depending on operating conditions and control strategies. For more information on the nature of cyclic variability, the reader can refer to other authors' works, e.g., [59,60].

Fig. 8 is a graphic depiction of how vibration and the HRR are phenomenologically corresponding to each other. To reject any bias related to averaging, further analyses are performed on an individual cycle basis, focusing on two pairs of synthetic parameters. This involves: (i) HRR$_{max}$ and amplitude of the first (positive) acceleration peak (Acc$_{max}$); and (ii) the CA-based location of the peak HRR (CA(HRR$_{max}$)) and the corresponding location of the first acceleration peak (CA (Acc$_{max}$)).

4.3. Determination of combustion timing, based on acceleration

The main takeaway from Fig. 8, discussed in the previous section, is that the CA(HRR$_{max}$) is correlated with the CA(Acc$_{max}$). However, the offset between the two variables tends to increase as the engine approaches higher speeds, due to the transfer path effect. Fig. 9 shows the correlation for all operating conditions, split into individual combustion cycles. As the individual cycles are grouped according to the rotational speed, the transfer path effect becomes evident. The locations are presented on the CA-basis, so at high speed there is a larger crankshaft rotation per vibration propagation time.

Fig. 9 also shows that when combustion is retarded, the Acc$_{max}$ signal precedes the HRR$_{max}$. This can be rationalised. As the combustion moves towards the expansion stroke, it slows down significantly and does not produce high PRR, giving a weak vibration amplitude. The outliers are thus the result of interference between the vibrations caused by compression and combustion, which are, in this case, of the same order of magnitude. In other words, the compression-induced vibration component shifts the peak acceleration towards TDC. Consequently, the situations where Acc$_{max}$ significantly precedes the HRR$_{max}$ manifest at low engine-speeds. The nonlinear effect of engine speed and the transfer path, thus deepens the apparent delta between both estimated parameters.

Table 5
Estimated regression coefficients of Eq. (5).

Parameter	Estimate	Std. Error	t_{obs}	p-value
α_0	−0.0703	0.2425	−0.2900	0.7742
α_1	$8.59 \bullet 10^{-4}$	0.0001	10.1591	$2 \bullet 10^{-10}$
α_2	−0.0634	0.3823	−0.1658	0.8696

Fig. 10 visualises the effect of rotational speed on the acceleration signal delay for all operating points. Here the delta between CA(Acc$_{max}$) and CA(HRR$_{max}$) is expressed as a median, calculated for each operating point independently. Evidently, there is a linear function expressing acceleration signal delay with zero-crossing at the $n = 0$ point. There is also a weak negative correlation between CA(Acc$_{max}$), CA(HRR$_{max}$) and IMEP, but it is statistically irrelevant.

To determine the level of significance of the operating conditions' influence on the estimated values, the linear model is considered in Eq.5.

$$\mathrm{CA(Acc_{max})} - \mathrm{CA(HRR_{max})} = \alpha_0 1 + \alpha_1 \bullet n + \alpha_2 \bullet \mathrm{IMEP} + \varepsilon \quad (5)$$

here, CA(Acc$_{max}$) – CA(HRR$_{max}$) is a (28-dimensional) vector of acceleration signal delaýs median values for 100 consecutive cycles. Note that we use the median as a quantifier to build the model because it is skewed by a small proportion of very small values, while the adjusted Fisher-Pearson skewness coefficient for all data equals −5.56 (refer to Appendix). There are two vectors of operational conditions in Eq. (5): rotational speed n and IMEP, while ε is a disturbance term. The results of the regression analysis for the formulated model are given in Table 5.

In Table 5, t_{obs} stands for the observed value of the t-distribution for testing the null hypothesis. The last column (p-value) shows the probabilities of obtaining test results at least as extreme as those actually observed. The obtained values allow one to verify the hypothesis that the coefficients α_0 and α_2 are both equal to 0. In other words, the IMEP dependency in Eq. (5) is statistically irrelevant, and the estimation of combustion timing indicators from vibration peak location can be modelled as a linear function with zero-crossing at 0 rpm, as foreseen by Fig. 10. Equation (6) formulates the established correlation for combustion timing CA(HRR$_{max}$) explicitly

$$\mathrm{CA(HRR_{max})} = \mathrm{CA(Acc_{max})} - \alpha_1 \bullet n \quad (6)$$

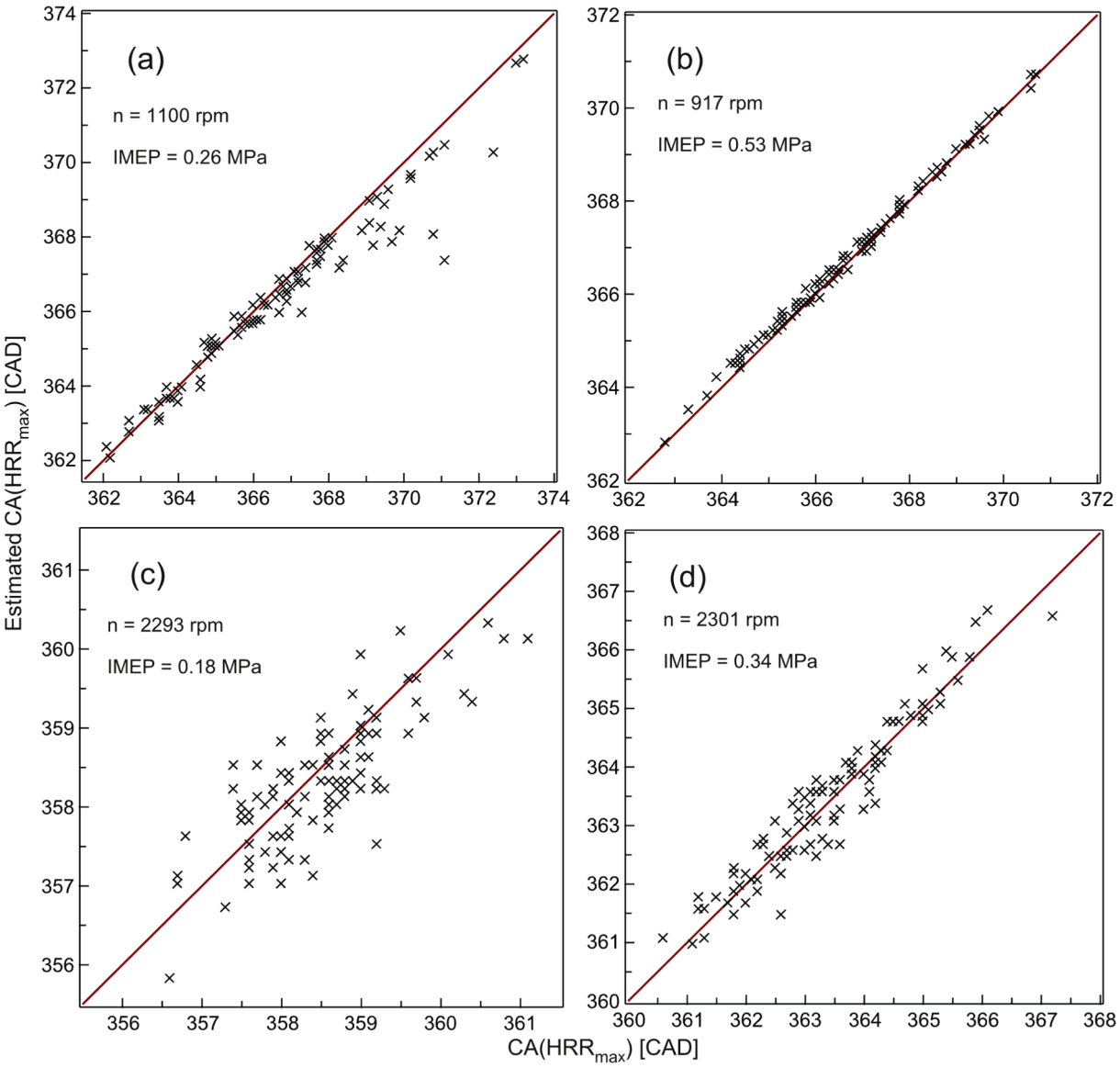

Fig. 11. Linear model of combustion timing from Eq. (6), compared to corresponding data obtained directly from the heat release analysis.

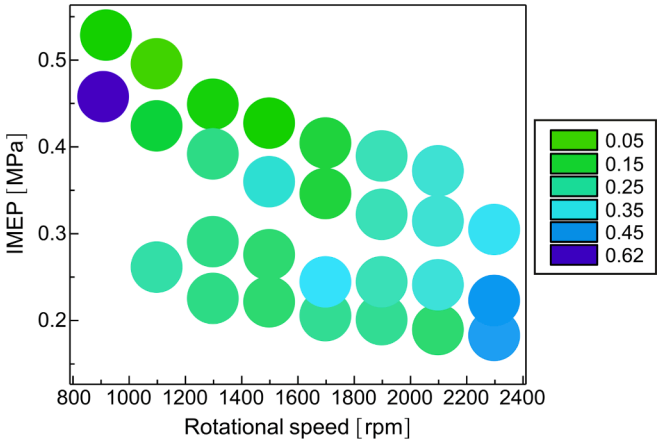

Fig. 12. Median absolute ([CAD]) error of the linear model of Eq. (6), for all operating points.

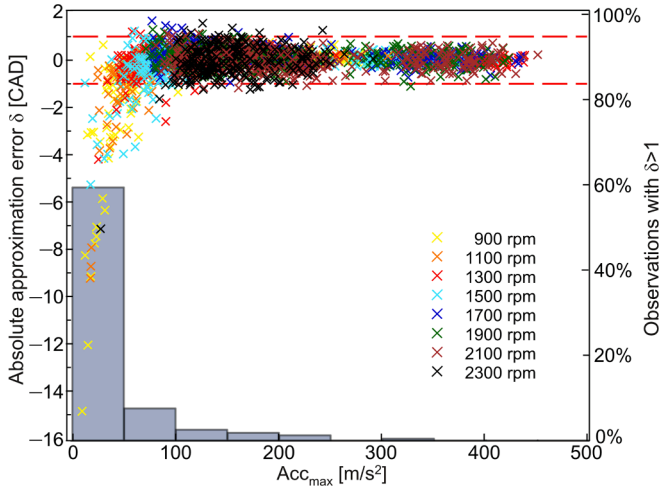

Fig. 13. Absolute error for combustion timing correlation (Eq.6) plotted vs. peak acceleration signal amplitude: all 100 cycles of selected worse-fitting operating points.

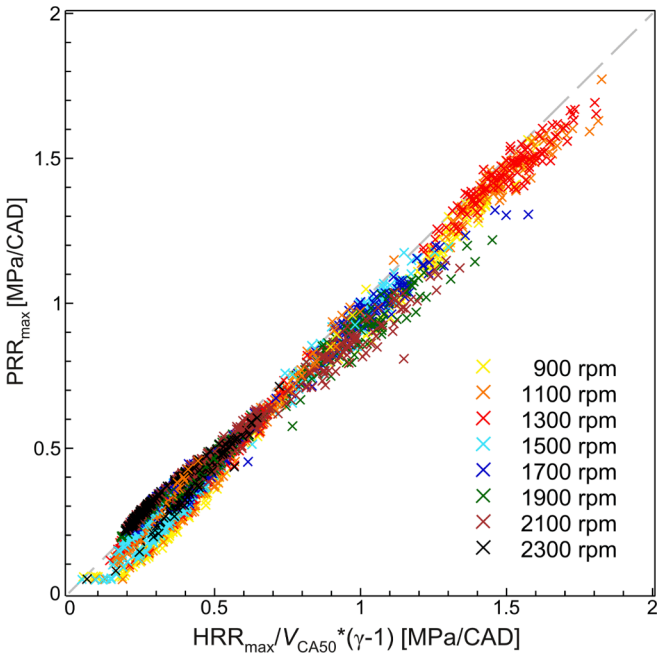

Fig. 14. Correlation of $HRR_{max}/V(CA50)*(\gamma-1)$ vs. PRR_{max}. The ratio of specific heat is assumed constant at $\gamma = 1.3$ for all operating points.

where $\alpha_1 = 8.59 \bullet 10^{-4}$ CAD/rpm.

Fig. 11 validates the above combustion timing correlation, on an individual cycle basis, for different speed/load conditions. Without any quantitative analysis, it is immediately apparent that the higher the engine load, the better the results. This relates to the already- mentioned phenomena. When less fuel energy is released, compression-induced vibrations start to interfere with the combustion-induced part of the spectrum. Both phenomena have similar frequencies and appear close to each other on the CA basis. Note, however, that the maximum error of combustion timing determination, at the lowest permissible engine loads, does not exceed ± 1 CAD.

Fig. 12 reveals that the CA(HRR_{max}) prediction error is determined also by other factors, aside from the governing engine-load influence. The model loses its accuracy at high speeds. This is plausible because compression pressure and inertia forces make a greater contribution to the vibration signal at high speeds, interfering with the combustion-borne signal. Additionally, the operating point with the highest combustion variability (n = 900 rpm, IMEP = 0.45 MPa) has the highest median absolute error of 0.62 CA.

Fig. 13 complements the picture, illustrating the mechanism of transferring combustion timing to peak vibration location, and the associated correlation uncertainties. The estimation error of CA (HRR_{max}) is plotted against the peak acceleration amplitudes. It can be seen, that independently of the speed and load, at low Acc_{max}, Eq. (6) underestimates the actual CA(HRR_{max}). It was already noted that it is the effect of phase shift by compression pressure and inertial forces, but Fig. 13 provides quantitative data on how the signal amplitude affects the estimation error. Combustion timing can be estimated within the error boundary of a single CAD where $Acc_{max} > 100$ m/s^2.

Note that ± 1 CAD is an accuracy attained by state-of-the-art, model-based combustion onset observers used in closed-loop LTC control [57]. Thus, the accuracy of the combustion timing determination methods presented here is considered sufficient for both in-cycle combustion control and load control on a mean-value basis, as soon as the threshold vibration signal amplitude is exceeded. This equates to 98.5% of the operating envelope. The method fails to establish a robust combustion control basis if the combustion is weak and slow, resulting in Acc_{max} values below 100 m/s^2. These situations pertain to the boundary of the feasible operating range, at low engine-speed and low loads.

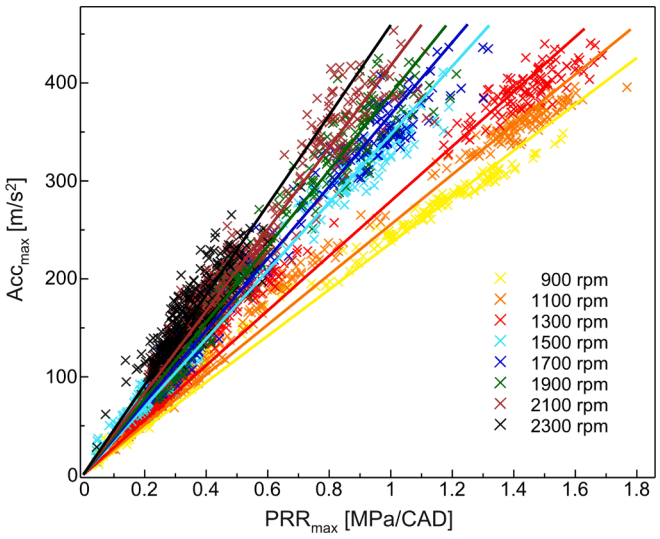

Fig. 15. The correlation of Acc_{max} and PRR_{max} expressed in the CA domain.

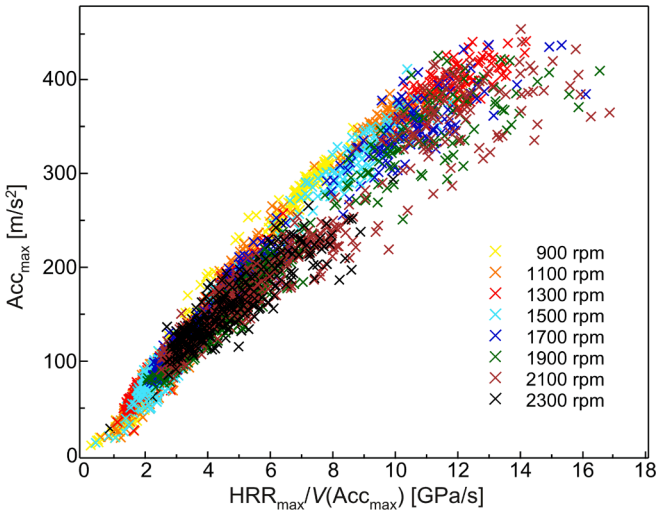

Fig. 16. Peak acceleration vs. $HRR_{max}/V(Acc_{max})$; note that the unit of HRR_{max} in this case is [MW].

4.4. Determination of peak HRR, based on acceleration

In the method section, we have argued that the amplitude of combustion-induced engine vibration is directly correlated to the peak PRR. This allows us to quasi-analytically relate it to the HRR, through Eq. (4). Fig. 14 validates the second part of this hypothesis, for all HCCI operating points in the test matrix. Note that, while deriving Eq. (4), it is assumed that the ratio of specific heats γ is constant across the combustion process, which is in line with the premise of the present work seeking a real-time method to determine HRR that is independent of in-cylinder pressure.

Fig. 14 confirms that PRR_{max} correlates well with HRR_{max} through Eq. (4). Higher discrepancies at low heat-release values result from a higher relative contribution of the volume derivative term in the first law analysis (Eq. (3), which Eq. (4) neglects. In this regime, the PRR will be overestimated for operating points with CA50 slightly before TDC. Consequently, cases with CA50 after TDC will be underestimated [49]. Again, note that neglecting the volume derivative term in Eq. (3) is necessary to eliminate the in-cylinder pressure from Eq. (4).

Table 6
Estimated regression coefficients of Eq. (7).

Parameter	Estimate	Std. Error	t_{obs}	p-value
β_0	0.8547	1.9157	0.4461	0.6593
β_1	0.0311	0.0009	32.9641	0
β_2	−0.0025	0.0052	−0.4774	0.6373

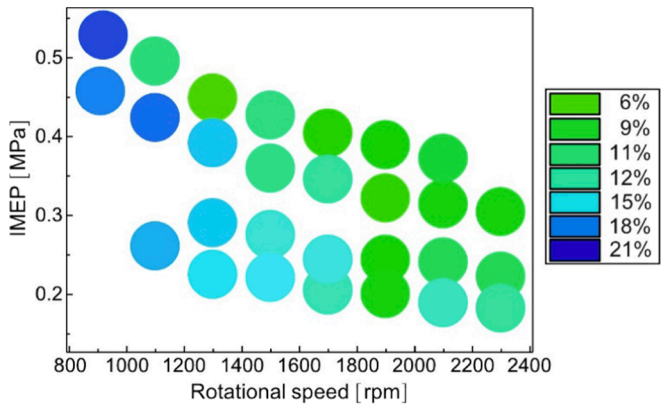

Fig. 17. Accuracy map (RME – relative mean error) of the model of the HRR_{max} prediction with Eq. (8).

As PRR is the direct combustion-induced excitation for vibration acceleration, then PRR_{max} and Acc_{max} should be bounded by an unknown transfer function, depending on the sensor location, engine-head design, material properties and temperature. To help determine this function indirectly, Fig. 15 shows how both parameters depend on each other on a cycle-averaged basis.

Fig. 15 proves good agreement between both values, but the effect of engine rotational speed can also be observed. This comes from the fact that PRR_{max} is expressed in the CA domain: changing to the time domain eliminates the engine-speed effect. Fig. 16 substitutes the time domain-expressed PRR values presented in Fig. 14 with the analytically-derived term relating it to the HRR (Eq. (4). In this transition, the constant-assumed gamma is abandoned, as it only acts as a linear scaling factor. Furthermore, the more fundamentally correct value of in-cylinder volume at the location of HRR_{max} presented explicitly in Eq. (4), is substituted with the corresponding volume at Acc_{max} for simplicity. As proven in the previous section, both locations correlate on the crank-angle basis, through a linear model of Eq. (6). It can be easily proven that, on the time-basis, the engine-speed term in Eq. (6) can be neglected, and thus this interposition is justified. The formal proof is omitted, as Fig. 16 shows the correctness of the above assumptions, without needing detailed analysis.

The correlation between Acc_{max} and HRR_{max} is evident from Fig. 16. It can be validated by considering the model in Eq. (7). It has been indirectly-proven, that on a time basis, the correlating phenomena do not significantly depend on engine-speed nor load. The statistical thesis that still needs to be verified, pertains to the dependency on disturbance (β_0) and the direct influence of the crank-angle term (β_2). Table 6 provides the results of the regression analysis for the model in Eq. (7)

$$HRR_{max} = \beta_0 1 + \beta_1 \bullet Acc_{max} \bullet V(Acc_{max}) + \beta_2 \bullet CA(Acc_{max}) \quad (7)$$

Based on the statistical tests quantifiers t_{obs} and p-value, the null hypothesis can be positively validated for parameters β_0 and β_2. Thus, the statistically-relevant model for estimating the amplitude of the peak HRR, based on the peak vibration amplitude, is as expressed in Eq. (8)

$$HRR_{max}[MW] = 0.031 \bullet Acc_{max}\left[\frac{m}{s^2}\right] \bullet V(Acc_{max})\left[cm^3\right] \quad (8)$$

Fig. 17 validates the model for all operating points on a cycle-averaged basis. The mean relative error for the estimated HRR_{max} reaches the maximum value of 21% for 900 rpm and 0.45 MPa IMEP. Partial burn cycles with weak HRR at this point mean the vibration component from imbalance and compression pressure is large in comparison to combustion-induced vibration. Interestingly, the estimation accuracy map in Fig. 17 does not overlap directly with the cycle-to-cycle variability map in Fig. 4.

The methods of the present study lack fundamental insight to investigate this issue thoroughly. Importantly however, from the applied point of view, the discussed HRR_{max} estimation error in all operating points is less than half the HCCI-inherited cycle-to-cycle variability levels presented in Fig. 4. Note, that the principle application for Eq. (8) is on-board, real-time determination of the boundaries of safe operation, from the perspective of mechanical and thermal stress induced by harsh combustion. Therefore, the control limits will have to be applied with a reasonable margin to allow for cycle-to-cycle variability. Taking these margins into account, the accuracy of peak HRR determination from the acceleration signal is considered sufficient from the perspective of the application.

5. Conclusions

The significant findings to emerge from the study can be summarised as follows:

- The spectral–temporal analysis allows separating combustion-borne vibrations from the rest of the engine spectrum, without advanced decomposition algorithms. Within the boundaries of attainable HCCI, the combustion spectrum is distinctive and does not overlap with other significant vibration sources such as the valvetrain, either in frequency or in the time domain. Combustion-attributed frequencies, independent of operating conditions, focus on 500 Hz bandwidth and appear in a crank-angle range between −10 CAD and 20 CAD after TDC firing.
- Focusing on the above window, the crank angle of peak vibration acceleration correlates with the crank angle of peak heat release rate (or 50% mass fuel burned), with a linear delay dependent on engine speed. To this end, the engine-speed term characterises the transfer function.
- The effect of other operating parameters on the transfer function is statistically irrelevant. Importantly, the form of the correlation is analytically derived and thus considered valid for all engines under the HCCI paradigm. There is only one tunable constant, which represents the propagation path through combustion chamber walls. This has to be established experimentally for a given engine mechanical design, but requires only minimum, single-point calibration effort.
- The proposed method can estimate HCCI, cycle-individual combustion timing from a one-directional vibration sensor, within a single crank-angle degree accuracy, as soon as the vibration amplitude is above the 100 m/s^2 threshold. That captures 98.5% of the operating envelope. The method is virtually instantaneous and, within the above validity constraints, can be used in real-time for closed-loop HCCI combustion control, in both cycle-to-cycle and in-cycle frameworks. The second feature is usually unattainable for conventional in-cylinder pressure-based combustion determination methods.
- Below the 100 m/s^2 threshold, the combustion acceleration feature interferes with vibrations induced by compression and piston inertia. This can happen only once every 10–20 well-predicted cycles, in operating conditions when HCCI reaches its boundaries of stable operation. In these rare events, the proposed method fails to establish robust HCCI combustion control on an individual cycle basis. Mean-value control (operating point transition) is still possible, as the median absolute combustion-timing prediction error per 100 cycles does not exceed 0.62 CAD for a worst-case scenario.

- The same framework allows identification of the peak HRR rates from the vibration signal amplitude. The equation, which is universally-valid for all HCCI engines, shows that both parameters correlate linearly, with cylinder volume as the scaling factor. The worst-case relative mean prediction error is high, at over 21%. However, taking into account the methods real-time capability, this is still sufficiently accurate to establish a targeted control action, based on a constraint limiter. Again, for 80% of the operating points, the HRR amplitude prediction error is of the same order as for the commonly applied in-cylinder pressure-based calculation.

CRediT authorship contribution statement

Jacek Hunicz: Conceptualization, Methodology, Investigation, Writing – original draft, Project administration, Funding acquisition, Supervision. **Michał S. Gęca:** Investigation, Resources, Data curation. **Elżbieta Ratajczyk:** Software, Formal analysis, Data curation, Visualization. **Amin Mahmoudzadeh Andwari:** Formal analysis, Writing – original draft. **Liping Yang:** Formal analysis, Writing – original draft, Writing – review & editing. **Maciej Mikulski:** Conceptualization, Writing – original draft, Writing – review & editing, Supervision, Funding acquisition.

Declaration of Competing Interest

The authors declare that they have no known competing financial interests or personal relationships that could have appeared to influence the work reported in this paper.

Data availability

Data will be made available on request.

Acknowledgements

The research was funded by the Lublin University of Technology statutory research, contract No. FD-20/IM-5/44. Maciej Mikulski acknowledges the support of the Silent Engine project co-funded by Business Finland (NextGenerationEU funding).

Appendix

All error quantifiers in Tables A1 and A2 are determined according to the same procedure. Skewness coefficients are calculated for 100 measurements in each operating condition. The model errors are reported in terms of mean signed deviation (MSD) and mean absolute error (MAE) for all operating conditions. The MSD allows verifying how the model predictions are biased from the true values in any direction under varying operating parameters, while the MEA measures the average magnitude of the errors without regard to their sign and it is a useful metric for evaluating the accuracy of the model. The adjusted Fisher-Pearson coefficient of skewness, for a given data $X_1, X_2, \ldots, X_n$, is defined by the formula:

$$G_1 = \frac{\sqrt{n(n-1)}}{n-2} \frac{\sum_{i=1}^{n} (X_i - \overline{X})^3 / n}{\mathrm{STD}^3},$$

where $\overline{X}$ is the mean value and STD is the standard deviation.

Table A1
Full regression analysis results for the model of CA(HRR_{max}) expressed by Eq. (6).

Rotational speed [rpm]	IMEP [MPa]	skewness coefficient	Mean of CA(Acc_{max}) [CAD]	STD of CA(Acc_{max}) [CAD]	MSD [CAD]	MAE [CAD]
910	0.46	−2.5	374.3	4.65	−1.54	1.71
917	0.53	−0.23	367.6	1.74	0.07	0.11
1110	0.26	−2.63	367.4	2.11	−0.37	0.47
1110	0.42	−4.06	370.8	4.28	−0.55	0.67
1110	0.49	−0.32	364	1.16	0.04	0.1
1309	0.22	−1.36	365.2	1.56	−0.10	0.30
1309	0.29	−0.64	365.1	1.66	−0.05	0.30
1308	0.39	−3.90	369.5	2.57	−0.10	0.34
1308	0.45	0.10	361.8	1.06	−0.03	0.10
1508	0.22	0.49	366.0	1.76	−0.04	0.31
1509	0.28	−1.27	367.3	2.16	−0.02	0.33
1506	0.36	−2.19	373.1	4.1	−0.60	0.71
1506	0.43	0.05	366	1.47	0.04	0.16
1705	0.20	0.20	362.6	1.26	0.16	0.29
1705	0.24	−0.14	364.5	1.57	0.19	0.35
1703	0.35	0.51	368.4	1.72	0.15	0.28
1703	0.40	−0.47	364.5	1.70	0.006	0.19
1903	0.20	0.50	361.8	1.36	0.11	0.31
1901	0.24	−0.26	363.7	1.35	0.20	0.36
1899	0.32	0.06	366.3	1.19	0.007	0.31
1899	0.39	−0.55	365	1.31	0.03	0.32
2098	0.19	0.19	360.6	1.03	0.02	0.31
2097	0.24	−0.38	362.7	1.04	0.14	0.37
2095	0.31	0.31	365.4	1.35	−0.19	0.39
2096	0.37	−0.17	364.5	1.15	−0.04	0.30
2293	0.18	0.14	360.3	0.81	−0.20	0.48
2291	0.22	−0.24	362.3	0.84	0.14	0.46
2291	0.30	−4.82	368.4	3.21	−0.12	0.5

Table A2
Full regression analysis results for the model of HRR_{max} expressed by Eq. (8).

Rotational speed [rpm]	IMEP [MPa]	Mean of HRR_{max} [GPa/s]	STD of HRR_{max}. [GPa/s]	MSD [GPa/s]	MAE [GPa/s]
910	0.46	0.39	0.19	0.02	0.19
917	0.53	1.29	0.15	−0.17	0.17
1110	0.26	0.34	0.07	−0.10	0.15
1110	0.42	0.72	0.25	−0.05	0.19
1110	0.49	1.84	0.15	−0.07	0.08
1309	0.22	0.35	0.05	−0.11	0.12
1309	0.29	0.36	0.06	−0.13	0.13
1308	0.39	0.77	0.16	−0.10	0.13
1308	0.45	2.18	0.19	0.004	0.04
1508	0.22	0.41	0.06	−0.10	0.12
1509	0.28	0.43	0.08	−0.09	0.11
1506	0.36	0.61	0.24	0.05	0.11
1506	0.43	1.63	0.21	−0.07	0.08
1705	0.20	0.51	0.06	−0.08	0.10
1705	0.24	0.62	0.08	−0.10	0.10
1703	0.35	0.94	0.14	−0.08	0.09
1703	0.40	1.95	0.29	0.02	0.06
1903	0.20	0.56	0.07	−0.002	0.07
1901	0.24	0.80	0.10	0.006	0.07
1899	0.32	1.10	0.12	0.03	0.07
1899	0.39	2.07	0.33	0.08	0.09
2098	0.19	0.59	0.06	−0.07	0.11
2097	0.24	0.91	0.11	−0.01	0.09
2095	0.31	1.33	0.19	0.09	0.11
2096	0.37	2.25	0.31	0.10	0.11
2293	0.18	0.63	0.07	−0.07	0.10
2291	0.22	0.88	0.12	0.0009	0.10
2291	0.30	1.10	0.28	0.07	0.10

References

[1] Reitz RD, Ogawa H, Payri R, Fansler T, Kokjohn S, Moriyoshi Y, et al. The future of the internal combustion engine. Int. J. Engine Res. 2019;21:3–10. https://doi.org/10.1177/1468087419877990.

[2] Krishnamoorthi M, Malayalamurthi R, He Z, Kandasamy S. A review on low temperature combustion engines: Performance, combustion and emission characteristics. Renew. Sustain. Energy Rev. 2019;116:109404. https://doi.org/10.1016/j.rser.2019.109404.

[3] Singh AP, Mustafi NN, Sharma YC, Agarwal AK. alternative fuels and their utilization strategies in internal combustion engines. Springer Nature Singapore 2020. https://doi.org/10.1007/978-981-15-0418-1_1.

[4] Saiteja P, Ashok B. A critical insight review on homogeneous charge compression ignition engine characteristics powered by biofuels. Fuel 2021;285:119202. https://doi.org/10.1016/J.FUEL.2020.119202.

[5] Yao M, Zheng Z, Liu H. Progress and recent trends in homogeneous charge compression ignition (HCCI) engines. Prog. Energy Combust. Sci. 2009;35:398–437. https://doi.org/10.1016/j.pecs.2009.05.001.

[6] Lu X, Han D, Huang Z. Fuel design and management for the control of advanced compression-ignition combustion modes. Prog. Energy Combust. Sci. 2011;37:741–83. https://doi.org/10.1016/j.pecs.2011.03.003.

[7] Duan X, Lai MC, Jansons M, Guo G, Liu J. A review of controlling strategies of the ignition timing and combustion phase in homogeneous charge compression ignition (HCCI) engine. Fuel 2021;285:119142. https://doi.org/10.1016/j.fuel.2020.119142.

[8] Telli GD, Altafini CR, Costa CA, Rosa JS, Martins ME, Oliveira Rocha LA. A comprehensive review of homogeneous charge compression ignition (HCCI) engines: Advantages, challenges and evolution. SAE Tech Pap 2020:2020-36-0042. https://doi.org/10.4271/2020-36-0042.

[9] Lang O, Salber W, Hahn J, Pischinger S, Hortmann K, Bücker C. Thermodynamical and mechanical approach towards a variable valve train for the controlled auto ignition combustion process. SAE Tech Pap 2005:2005-01-0762. https://doi.org/10.4271/2005-01-0762.

[10] Valero-Marco J, Lehrheuer B, López JJ, Pischinger S. Potential of water direct injection in a CAI/HCCI gasoline engine to extend the operating range towards higher loads. Fuel 2018;231:317–27. https://doi.org/10.1016/j.fuel.2018.05.093.

[11] Kokjohn SL, Hanson RM, Splitter DA, Reitz RD. Fuel reactivity controlled compression ignition (RCCI): A pathway to controlled high-efficiency clean combustion. Int. J. Engine Res. 2011;12:209–26. https://doi.org/10.1177/1468087411401548/asset/images/large/10.1177_1468087411401548-fig2.jpeg.

[12] Rosa JS, Martins MES, Telli GD, Altafini CR, Wander PR, Rocha LAO. Exploring the effects of diesel start of injection and water-in-ethanol concentration on a reactivity controlled compression ignition engine. Fuel 2020;281:118751. https://doi.org/10.1016/j.fuel.2020.118751.

[13] Tartakovsky L, Sheintuch M. Fuel reforming in internal combustion engines. Prog. Energy Combust. Sci. 2018;67:88–114. https://doi.org/10.1016/j.pecs.2018.02.003.

[14] Hunicz J, Mikulski M. Investigation of the thermal effects of fuel injection into retained residuals in HCCI engine. Appl. Energy 2018;228:1966–84. https://doi.org/10.1016/j.apenergy.2018.07.075.

[15] Maurya RK, Agarwal AK. Investigations on the effect of measurement errors on estimated combustion and performance parameters in HCCI combustion engine. Measurement 2013;46:80–8. https://doi.org/10.1016/j.measurement.2012.05.021.

[16] Ulrich O, Wlodarczyk R, Wlodarczyk MT. High-accuracy low-cost cylinder pressure sensor for advanced engine controls. SAE Tech Pap 2001:2001-01-0991. https://doi.org/10.4271/2001-01-0991.

[17] Jardine AKS, Lin D, Banjevic D. A review on machinery diagnostics and prognostics implementing condition-based maintenance. Mech. Syst. Sig. Process. 2006;20:1483–510. https://doi.org/10.1016/j.ymssp.2005.09.012.

[18] Delvecchio S, Bonfiglio P, Pompoli F. Vibro-acoustic condition monitoring of internal combustion engines: A critical review of existing techniques. Mech. Syst. Sig. Process. 2018;99:661–83. https://doi.org/10.1016/j.ymssp.2017.06.033.

[19] Wang Z, Liu H, Reitz RD. Knocking combustion in spark-ignition engines. Prog. Energy Combust. Sci. 2017;61:78–112. https://doi.org/10.1016/j.pecs.2017.03.004.

[20] Lee S, Lee Y, Lee S, Song HH, Min K, Choi H. Study on the correlation between the heat release rate and vibrations from a diesel engine block. SAE Tech Pap 2015:2015-01-1673. https://doi.org/10.4271/2015-01-1673.

[21] Zhao X, Cheng Y, Wang L, Ji S. Real time identification of the internal combustion engine combustion parameters based on the vibration velocity signal. J. Sound Vib. 2017;390:205–17. https://doi.org/10.1016/j.jsv.2016.11.013.

[22] Yang W, Yong C. Vibration analysis and combustion parameter evaluation of CI engine based on fourier decomposition method. Int. J. Engine Res. 2022;23:434–45. https://doi.org/10.1177/1468087420988195/asset/images/large/10.1177_1468087420988195-fig2.jpeg.

[23] Schaberg PW, Priede T, Dutkiewicz RK. Effects of a rapid pressure rise on engine vibration and noise. SAE Tech Pap 1990;900013. https://doi.org/10.4271/900013.

[24] Chiatti G, Chiavola O, Recco E, Magno A, Mancaruso E, Vaglieco BM. Accelerometer measurement for MFB evaluation in multi-cylinder diesel engine. Energy 2017;133:843–50. https://doi.org/10.1016/j.energy.2017.04.148.

[25] Badawi B, Elmaihy A, Samy S, Shahin AMK. Reconstruction of diesel engine cylinder pressure using vibration and acoustic emission. Int Conf Appl Mech Mech Eng 2006;12:510–25. https://doi.org/10.21608/amme.2006.41368.

[26] Gao Y, Randall RB. Reconstruction of diesel engine cylinder pressure using a time domain smoothing technique. Mech. Syst. Sig. Process. 1999;13:709–22.

[27] El-Ghamry M, Steel JA, Reuben RL, Fog TL. Indirect measurement of cylinder pressure from diesel engines using acoustic emission. Mech. Syst. Sig. Process. 2005;19:751–65. https://doi.org/10.1016/j.ymssp.2004.09.004.

[28] Antoni J, Daniere J, Guillet F. Effective vibration analysis of IC engines using cyclostationarity. Part I-A methodology for condition monitoring. J. Sound Vib. 2002;257:815–37. https://doi.org/10.1006/jsvi.2002.5062.

[29] Antoni J, Daniere J, Guillet F, Randall RB. Effective vibration analysis of IC engines using cyclostationarity. Part II—New results on the reconstruction of the cylinder pressures. J. Sound Vib. 2002;257:839–56. https://doi.org/10.1006/jsvi.2002.5063.

[30] Grover Zurita V, Haupt D, Ågren A. Reconstruction of cylinder pressure through multivariate data analysis: For prediction of noise and exhaust emissions. Noise Control Eng J 2004;52:154–63. https://doi.org/10.3397/1.2839745.

[31] Peña JC, Zurita G. Vibration based reconstruction of the cylinder pressure in diesel engines by using neural networks. Rev Investig Desarro 2005;1:81–9.

[32] Bizon K, Continillo G, Mancaruso E, Vaglieco BM. Reconstruction of In-cylinder pressure in a diesel engine from vibration signal using a RBF neural network model. SAE Tech Pap 2011:2011-24-0161. https://doi.org/10.4271/2011-24-0161.

[33] Johnsson R. Cylinder pressure reconstruction based on complex radial basis function networks from vibration and speed signals. Mech. Syst. Sig. Process. 2006;20:1923–40. https://doi.org/10.1016/j.ymssp.2005.09.003.

[34] Trimby S, Dunne JF, Bennett C, Richardson D. Unified approach to engine cylinder pressure reconstruction using time-delay neural networks with crank kinematics or block vibration measurements. Int. J. Engine Res. 2017;18:256–72. https://doi.org/10.1177/1468087416655013.

[35] Maurya RK. Characteristics and Control of Low Temperature Combustion Engines. ISBN: 978-3-319-68507-6, 2018. https://doi.org/10.1007/978-3-319-68508-3.

[36] Cheng Y, Tang J, Ji S, Huang M. Combustion timing determination based on vibration velocity in HCCI engines. Mech. Mach. Theory 2012;58:20–8. https://doi.org/10.1016/j.mechmachtheory.2012.08.004.

[37] Chauvin J, Grondin O, Nguyen E, Guillemin F. Real-time combustion parameters estimation for HCCI-diesel engine based on knock sensor. Measurement 2008;vol. 41:IFAC. https://doi.org/10.3182/20080706-5-kr-1001.01437.

[38] Grondin O, Chauvin J, Guillemin F, Nguyen E, Corde G. Combustion parameters estimation and control using vibration signal : Application to the diesel HCCI engine. Proc IEEE Conf Decis Control 2008:5621–7. https://doi.org/10.1109/CDC.2008.4739301.

[39] Nguyen HK, Modabberian A, Zenger K, Lendormy É, Mikulski M, Hunicz J. A Neural network approach for reconstructing in-cylinder pressure from engine vibration data. SAE Tech Pap 2022:2022-01-1038. https://doi.org/10.4271/2022-01-1038.

[40] Ji S, Li Y, Tian G, Ma R, Shu M, Zhang S, et al. Study on the relationship between combustion parameters and cylinder head vibration signal in time domain. Energies 2021;14:6421. https://doi.org/10.3390/EN14196421.
[41] Azzoni P. Reconstruction of indicated pressure waveform in a spark-ignition engine from blocic vibration measurements. J Dyn Syst Meas Control Trans ASME 1997; 119:614–9. https://doi.org/10.1115/1.2802369.
[42] Massey JA, Drallmeier JA, Eaton SJ, Wagner RM. Influence of the combustion energy release on surface accelerations of an HCCI engine. SAE Tech Pap 2009: 2009-01-2741. https://doi.org/10.4271/2009-01-2741.
[43] Bizon K, Continillo G, Mancaruso E, Vaglieco BM. Towards on-line prediction of the in-cylinder pressure in diesel engines from engine vibration using artificial neural networks. SAE Tech Pap 2013:2013-24-0137. https://doi.org/10.4271/2013-24-0137.
[44] Grajales JA, Quintero HF, Romero CA, Henao E, López JF, Torres D. Combustion pressure estimation method of a spark ignited combustion engine based on vibration signal processing. J Vibroengineering 2016;18:4237–47. https://doi.org/10.21595/JVE.2016.17311.
[45] Ji S, Lan X, Lian J, Wang H, Li M, Cheng Y, et al. Combustion parameter estimation for ICE from surface vibration using frequency spectrum analysis. Measurement 2018;128:485–94. https://doi.org/10.1016/J.MEASUREMENT.2018.07.002.
[46] Han R, Bohn C, Bauer G. Recursive engine in-cylinder pressure estimation using kalman filter and structural vibration signal. IFAC-PapersOnLine 2018;51:700–5. https://doi.org/10.1016/j.ifacol.2018.10.161.
[47] Hunicz J. On cyclic variability in a residual effected HCCI engine with direct gasoline injection during negative valve overlap. Math. Probl. Eng. 2014;2014. https://doi.org/10.1155/2014/359230.
[48] Mauro S, Şener R, Gül MZ, Lanzafame R, Messina M, Brusca S. Internal combustion engine heat release calculation using single-zone and CFD 3D numerical models. Int. J. Energy Environ. Eng. 2018;9:215–26. https://doi.org/10.1007/S40095-018-0265-9/FIGURES/11.
[49] Hunicz J, Mikulski M, Geca MS, Rybak A. An applicable approach to mitigate pressure rise rate in an HCCI engine with negative valve overlap. Appl. Energy 2020;257:114018. https://doi.org/10.1016/j.apenergy.2019.114018.
[50] Jia M, Xie M, Liu H, Lam WH, Wang T. Numerical simulation of cavitation in the conical-spray nozzle for diesel premixed charge compression ignition engines. Fuel 2011;90:2652–61. https://doi.org/10.1016/j.fuel.2011.04.017.
[51] Torrence C, Compo P. A practical guide to wavelet analysis. Bull. Am. Meteorol. Soc. 1998:61–78. https://doi.org/10.1175/1520-0477(1998)079.
[52] Sen AK, Litak G, Taccani R, Radu R. Wavelet analysis of cycle-to-cycle pressure variations in an internal combustion engine. Chaos Solitons Fractals 2008;38: 886–93. https://doi.org/10.1016/J.chaos.2007.01.041.
[53] Sen AK, Litak G, Yao BF, Li GX. Analysis of pressure fluctuations in a natural gas engine under lean burn conditions. Appl. Therm. Eng. 2010;30:776–9. https://doi.org/10.1016/j.applthermaleng.2009.11.002.
[54] Bachman G, Narici L, Beckenstein E. Fourier and Wavelet Analysis. ISBN: 978-1-4612-6793-5, 2000. https://doi.org/10.1007/978-1-4612-0505-0.
[55] Härdle WK, Simar L. Applied multivariate statistical analysis. Springer Cham 2019. https://doi.org/10.1007/978-3-030-26006-4.
[56] Scaringe R, Wildman CB, Cheng WK. On the high load limit of boosted gasoline HCCI engine operating in NVO mode. SAE Int. J. Engines 2010;3:35–45. https://doi.org/10.4271/2010-01-0162.
[57] Sakhaei B, Durali M. Vibration transfer path analysis and path ranking for NVH optimization of a vehicle interior. Shock Vib. 2014;2014. https://doi.org/10.1155/2014/697450.
[58] Lee C, Tomita E, Lee K. Characteristics of combustion stability and emission in SCCI and CAI combustion based on direct-injection gasoline engine. SAE Tech Pap 2007: 2007-01-1872. https://doi.org/10.4271/2007-01-1872.
[59] Hunicz J, Geca M, Rysak A, Litak G, Kordos P. Combustion timing variability in a light boosted controlled auto-ignition engine with direct fuel injection. J Vibroengineering 2013;15:1093–101.
[60] Hunicz J, Mikulski M, Koszałka G, Ignaciuk P. Detailed analysis of combustion stability in a spark-assisted compression ignition engine under nearly stoichiometric and heavy EGR conditions. Appl. Energy 2020;280:115955. https://doi.org/10.1016/j.apenergy.2020.115955.